BRNO UNIVERSITY OF TECHNOLOGY
VYSOKÉ UČENÍ TECHNICKÉ V BRNĚ

FACULTY OF MECHANICAL ENGINEERING
FAKULTA STROJNÍHO INŽENÝRSTVÍ

INSTITUTE OF PHYSICAL ENGINEERING
ÚSTAV FYZIKÁLNÍHO INŽENÝRSTVÍ

SPATIAL CONFINEMENT EFFECTS IN METAMAGNETIC NANOSTRUCTURES

VLIV PROSTOROVÉHO OMEZENÍ NA VLASTNOSTI METAMAGNETICKÝCH NANOSTRUKTUR

MASTER'S THESIS
DIPLOMOVÁ PRÁCE

AUTHOR — **Bc. Jiří Jaskowiec**
AUTOR PRÁCE

SUPERVISOR — **Ing. Vojtěch Uhlíř, Ph.D.**
VEDOUCÍ PRÁCE

BRNO 2019

BRNO UNIVERSITY OF TECHNOLOGY
FACULTY OF MECHANICAL ENGINEERING

Specification Master's Thesis

Department:	Institute of Physical Engineering
Student:	**Bc. Jiří Jaskowiec**
Study programme:	Applied Sciences in Engineering
Study field:	Physical Engineering and Nanotechnology
Supervisor:	**Ing. Vojtěch Uhlíř, Ph.D.**
Academic year:	2018/19

Pursuant to Act no. 111/1998 concerning universities and the BUT study and examination rules, you have been assigned the following topic by the institute director Master's Thesis:

Spatial confinement effects in metamagnetic nanostructures

Concise characteristic of the task:

First–order magneto–structural phase transition in FeRh thin films is associated with a nucleation mechanism which shows critical behavior typically observed for phase transitions of the second order. This behavior will be studied using magnetic force microscopy for nanostructures of different sizes, which also show a strong asymmetry of the phase transition between heating and cooling. Stochastic nucleation of the antiferromagnetic phase in the supercooled state of the nanostructures will be investigated using electrical transport measurements.

Goals Master's Thesis:

1. Imaging and quantitative analysis of phase domains for different nanostructure size.
2. Analysis of stochastic nucleation of FeRh antiferromagnetic phase in the supercooled state of nanostructures.

Recommended bibliography:

COEY, J. M. D. (2009): Magnetism and Magnetic Materials. Cambridge University Press, Cambridge.

PAPON, P., LEBLOND, J. a MEIJER, P. H. E. : The physics of phase transitions. Springer-Verlag Berlin Heidelberg, (2006).

MANEKAR, M., MUKHERJEE, C. a ROY, S. B. : Imaging of time evolution of the first-order magneto-structural transition in Fe-Rh alloy using magnetic force microscopy. Europhysics Letters, vol. 80, pp. 17004, DOI: 10.1209/0295-5075/80/17004, (2007).

UHLÍŘ, V., ARREGI, J. A. a FULLERTON, E. E. : Colossal magnetic phase transition asymmetry in mesoscale FeRh stripes. Nature Communications, vol. 7, pp. 13113, DOI: 10.1038/ncomms13113, (2016).

Deadline for submission Master's Thesis is given by the Schedule of the Academic year 2018/19

In Brno,

L. S.

prof. RNDr. Tomáš Šikola, CSc.
Director of the Institute

doc. Ing. Jaroslav Katolický, Ph.D.
FME dean

Summary
New properties and effects caused by spatial confinement of materials have critical influence in many scientific and technical fields. Reduction of device sizes, increase of recording density and increasing process efficiency are current trends in electronic industry. In this work, the influence of spatial confinement on the metamagnetic phase transition in Iron-Rhodium (FeRh) is studied. The FeRh alloy exhibits a first order phase transition from the antiferromagnetic phase to the ferromagnetic phase. Using magnetic force microscopy in an out-of-plane magnetic field the phase domain structure is imaged and analyzed across the phase transition. Quantitative analysis of measured data is done using the height-height correlation function and its results are compared for different structure sizes and thin layer thicknesses.

Abstrakt
Silné prostorové omezení materiálů způsobuje jejich nové vlastnosti, které mohou najit uplatnění v mnoha vědeckých i technických odvětvích. Snaha zmenšit velikosti součástek, zvětšit hustotu zápisu a zefektivnit procesy je současným trendem elektronického průmyslu. V této práci je studován vliv prostorového omezení na vlastnosti metamagnetického železo-rhodia (FeRh) během fázové přeměny. FeRh je materiál vykazující fázovou přeměnu prvního druhu mezi antiferomagnetickou a feromagnetickou fází. Metodou mikroskopie magnetických sil v magnetickém poli kolmém na rovinu vzorku je zobrazeni a analyzována struktura fázových domén behem fázové přeměny. Kvantitativní analýza naměřených dat je provedena užitím výškové korelační funkce a její výsledky jsou porovnány pro různé velikosti struktur a tloušťky tenkých vrstev.

Keywords
iron-rhodium, magnetic force microscopy, phase transition, antiferromagnetism, ferromagnetism, spatial confinement, height-height correlation function

Klíčová slova
železo-rhodium, mikroskopie magnetických sil, fázová přeměna, antiferomagnetismus, feromagnetismus, prostorové omezení, výšková korelační funkce

JASKOWIEC, Jiří. *Spatial confinement effects in metamagnetic nanostructures*. Brno, 2019. 55 pp. Master's thesis. Brno University of Technology. Faculty of Mechanical Engineering. Supervised by Vojtěch UHLÍŘ.

I hereby declare that I have written my master's thesis on theme of *Spatial confinement effects in metamagnetic nanostructures* independently, under the guidance of the master's thesis supervisor, Ing. Vojtěch Uhlíř, Ph.D., and using the technical literature and other sources of information which are all properly quoted in the thesis and detailed in the list of literature at the end of the thesis.

Bc. Jiří Jaskowiec

Mé díky patří vedoucímu práce Ing. Vojtěchu Uhlíři, Ph. D. za vzorné vedení mé práce, za podnětné připomínky, korektury a trpělivý přístup. Ing. Vojtěchu Schánilcovi děkuji za optimalizaci teplotního modulu pro MFM a za veškerou poskytnutou podporu. Mgr. Jiřímu Liškovi, Ph. D., a M. Sc. Jonimu Anderu Arregimu Uribeetxebarriovi, Honzovi Hajdučkovi6 děkuji za přípravu vzorku a jejich VSM analýzu. Ing. Michalu Horkému a Dr. Ing. Michalu Staňovi děkuji nejen za pomoc v poslední fázi práce, zejména však za provedení litografických kontaktů a optimalizaci detekce skokové fázové přeměny, respektive. Bc. Kataríně Rovenské děkuji za všechny korektury a podporu. Děkuji všem členům magnetické skupiny za vstřícný a přátelský přístup, jmenovitě inženýrům Igoru Turčanovi, Marku Vaňatkovi a Lukáši Flajšmanovi děkuji za vždy nataženou pomocnou ruku, veškeré rady a za vytvoření pozitivní atmosféry.
Své rodině, rodičům, sourozencům a jejim partnerům děkuji za podporu během celého studia, speciálně své sestře Lence za poskytnutí zázemí, přímou podporu a veškerou pomoc nejen během vypracovávání diplomové práce.

Děkuji mnohokrát všem lidem v mém okolí, bez vás by tato práce nemohla nikdy vzniknout.

Bc. Jiří Jaskowiec

Part of the work was carried out with the support of CEITEC Nano Research Infrastructure (ID LM2015041, MEYS CR, 2016–2019), CEITEC Brno University of Technology.

Contents

Introduction

Phase transitions are all around us and in the daily life, the most common example is the phase transforming water. Despite the familiar nature and ubiquity of water in our environment the associated phase transitions are not trivial to explain due to the peculiar properties of water, such as the anomaly in density at 4 °C. However, general properties of phase transitions can be better characterized in material classes featuring solid-state transitions.

The prototypical transition for this work is the metamagnetic phase transition in Iron-Rhodium (FeRh) and the method of observation is Magnetic Force Microscopy (MFM). The equiatomic FeRh alloy is antiferromagnetic (AF) at room temperature and during the heating, FeRh exhibits a phase transition to the ferromagnetic state (FM) [1]. The transition temperature being close to the room temperature is not only convenient for fundamental studies, but also for applications in sensing, magnetic refrigeration [2] and Heat-Assisted Magnetic Recording (HAMR) [3, 4], which can increase the density of recording. The confinement of FeRh to submicron structures may bring new emergent phenomena [5] – such as the abrupt phase transition during cooling.

Experimental part of this work deals with the spatial confinement effects on the phase transition featured in the domain structure. The effect of supercooling is shown to depend on the structure size and the amount of nucleation centers. The next studied effect is connected to the variable thickness of FeRh films. A significant part of the work deals with optimizing the approaches to obtain quantitative information about the phase domain sizes during the transition using the Height-Height Correlation Functions (HHCF).

This master's thesis is the direct follower of the previous works [6, 7] dealing with a related topic – imaging of the phase transition by MFM. The master's thesis summarizes last three years of this topic study in the Nanomagnetism and Spintronics group at CEITEC BUT.

1. Magnetism and phase transitions

It is well-known that electrons possess inherent properties called mass[1] and electrical charge[2]. For scientists and engineers studying magnetism, the more important property of an electron is its contribution to the total angular momentum, called spin. [8] In addition to the spin angular momentum, there is a contribution connected to the motion of an electron around the nucleus, denoted as an orbital angular momentum. These two components may be coupled by spin–orbit interaction to form the total electronic angular momentum [9] which is according to Einstein–de Haas effect proportional to magnetic moment $\vec{\mu}$. [10] Magnetization is then defined as the vector sum of all magnetic moments in the material divided by the material volume V

$$\vec{M} = \frac{1}{V} \sum_{i=1}^{N} \vec{\mu}_i \,, \tag{1.1}$$

where N is the number of magnetic moments.

1.1. Magnetic energies

The magnetization in a material is not generally uniform and varies from point to point. [11] At special circumstances, for instance when a magnetic material is formed to a structure with characteristic dimensions below 200 nm, uniform magnetization of the structure occurs. [12] Such an uniformly magnetized structure is shown in Figure 1.1a. A more complex double-vortex structure is depicted in Figure 1.1b. [11] In this example the force

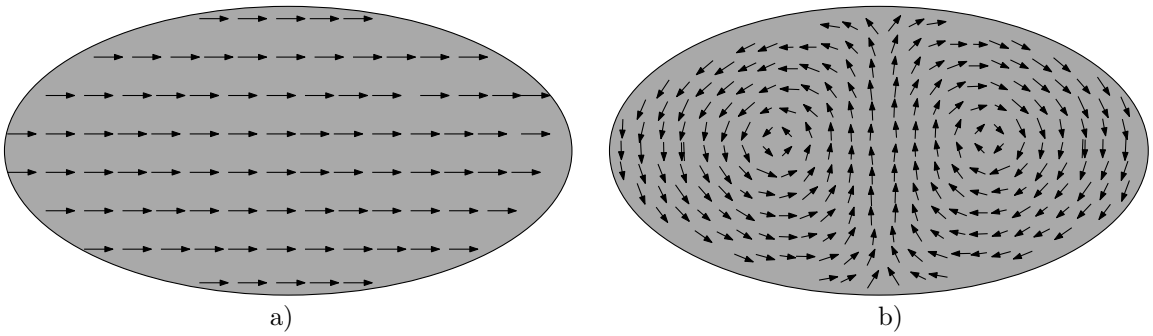

Figure 1.1: Example of domain structure of a) Single domain where is uniform magnetization. b) Double vortex domain structure. Adapted from [11]

keeping the magnetic moments colinear is overcome by a different force (which increases

[1] $m_e \approx 9.1 \times 10^{-31}\,\mathrm{kg}$
[2] $e \approx 1.6 \times 10^{-16}\,\mathrm{C}$

with the size of the structure), resulting in the double-vortex state. The stable state of the system is always a result of minimizing the total free energy of the system. The main contributions to the total free energy are the exchange energy, the dipolar energy, the anisotropy energy and the Zeeman energy.

1.1.1. Exchange energy

The long-range magnetic order is formed by the exchange interaction which has an origin in the electrostatic interaction and the Pauli's exclusion principle. The exchange interaction is described by a Heisenberg Hamiltonian [10]

$$H_{\mathrm{ex}} = -\sum_{i,j} J_{ij}\ \vec{S}_i \cdot \vec{S}_j, \tag{1.2}$$

where $\vec{S}_i$ and $\vec{S}_j$ are two neighboring spins and J_{ij} is exchange interaction constant – the so-called exchange stiffness. This interaction is responsible for the parallel orientation of the neighboring spins. If $J > 0$, it leads to ferromagnetic order, more discussed in the section 1.2. Otherwise, $J < 0$ leads to antiferromagnetic order, discussed in the section 1.3. [9]

1.1.2. Zeeman energy

When external magnetic field $\vec{B}_{\mathrm{ext}}$ is applied, another contribution to the total magnetic energy, called Zeeman energy, is introduced. The external magnetic field $\vec{B}_{\mathrm{ext}}$ tends to align magnetic moments $\vec{\mu}$ along its direction. This could be mathematically written as

$$E_{\mathrm{z}} = -\vec{\mu} \cdot \vec{B}_{\mathrm{ext}}. \tag{1.3}$$

The system of magnetic moments $\vec{\mu}$ has minimal Zeeman energy when all magnetic moments $\vec{\mu}$ are parallel to the external field $\vec{B}_{\mathrm{ext}}$. The net force acting on a magnetic moment $\vec{\mu}$ could be then obtained as:

$$\vec{F}_{\mathrm{z}} = \nabla(\vec{\mu} \cdot \vec{B}_{\mathrm{ext}}). \tag{1.4}$$

This equation is useful in the Magnetic Force Microscopy technique where a magnetized tip, representing a magnetic moment, interacts with the stray field of the sample; causing attraction or repulsion of the tip, as will be further discussed in the section dedicated to MFM. 3.2

1.1.3. Demagnetizing energy

Each magnetic moment in a material is a source of magnetic field. The vector sum of magnetic fields produced by all magnetic moments is called the dipolar field $\vec{B}_{\mathrm{dipolar}}$. THe magnetic dipolar field outside the sample is called the magnetic stray field $\vec{B}_{\mathrm{stray}}$, inside the sample it is denoted as the demagnetizing field $\vec{B}_{\mathrm{demag}}$. [9, 10] The demagnetizing energy is then described as a Zeeman-like interaction of the magnetization and the demagnetizing field

$$E_{\mathrm{demag}} = -\frac{1}{2V} \iiint_V \vec{M} \cdot \vec{B}_{\mathrm{demag}}\, \mathrm{d}V\,, \tag{1.5}$$

in a continuum approximation where $\vec{M}$ is the sample magnetization.

1.1.4. Anisotropy energy

Generally, there are two types of magnetic anisotropies. The first type is connected with the shape of the sample and originates from minimization of the demagnetizing energy. For instance, this causes the magnetization in a cylindrical shaped sample to prefer the orientation along the long axis. The same follows in a thin layer, where magnetization prefers to orient in-plane.

The other type of anisotropy is the crystalline anisotropy connected to the preferential directions in a crystal lattice called the easy axes. For instance, cobalt crystallizes in the hexagonal close-packed lattice type, hence the magnetization prefers to orient along the easy axis in the direction [0001].

The simplest case corresponds to the uniaxial anisotropy energy

$$E_{\mathrm{u}} = \frac{1}{V} \iiint_V K_{\mathrm{u}} \sin^2 \vartheta \, \mathrm{d}V, \tag{1.6}$$

where ϑ is the angle between the easy axis and the direction of magnetization $\vec{M}$. K_{u} stands for the uniaxial anisotropy constant. The axis perpendicular to the easy axis ($\vartheta = = 90°$) is termed as the hard axis and the uniaxial energy has its maximum in this direction. It should be mentioned that measuring[3] K_{u} is by principle easier than measuring other magnetic constants, such as exchange stiffness J.

1.1.5. Competing energies

The stable state is always corresponding to the minimum of total magnetic energy. In previous sections four basic contributions to the total magnetic energy, the exchange energy, Zeeman energy, dipolar energy and anisotropy energy were introduced. The individual energies influence the resulting domain structure, as shown in the Figure 1.2 – the presented data were simulated using mumax[4] in a square ferromagnetic element. [13] Influence of the exchange interaction is shown in Figure 1.2a. The energetic minimum corresponds to the parallel orientation of all spins which results in a single domain structure. In Figure 1.2b the dipolar energy was "activated". The result is formation of four domains and domain walls in a so-called Landau pattern. The Zeeman energy is "activated" in Figure 1.2c with magnetic field $\vec{B}_{\mathrm{ext}}$ applied in the horizontal direction as indicated in the Figure. It leads to expansion of the domains oriented parallel to the external field at the expense of the antiparallel oriented ones. At last in Figure 1.2d, anisotropy with an easy axis in the vertical direction takes its role, leading to the expansion of vertical domains and the reduction of the horizontal ones.

Besides these four basic energies, there are other energies relevant for the resulting magnetic configuration, such as more complicated exchange energy terms, e.g. Dzyaloshinskii–Moriya, billinear and biquadratic forms of the exchange interaction. More information could be found in the dedicated magnetism textbooks as [9–12].

[3] For example by measuring hysteresis loops in easy and in hard axis by Vibrating Sample Magnetometry.

[4] `http://mumax.github.io/`

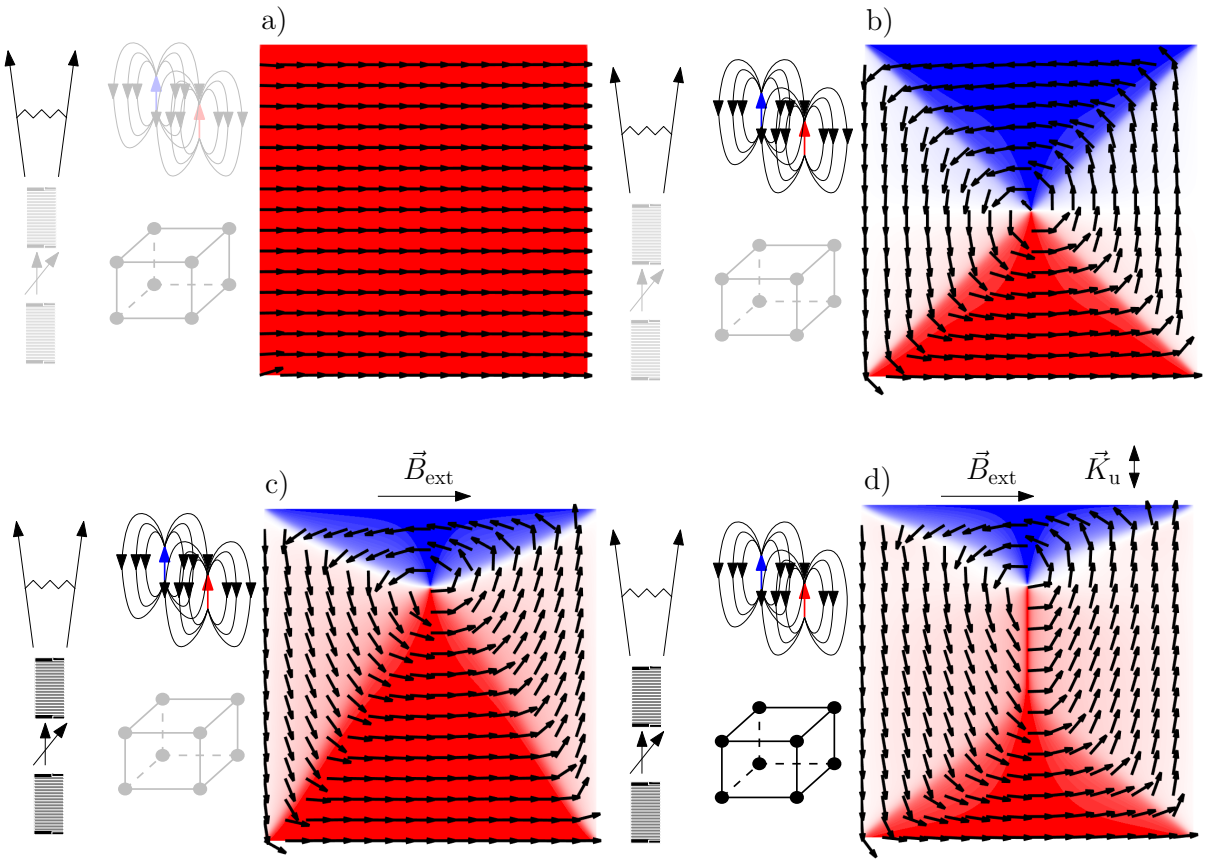

Figure 1.2: Results of the micromagnetic simulations in mumax for ferromagnetic square element when different contributors to total energy are consequently "turned on". a) Result of the simulation with only exchange interaction. b) Result of the simulation with added dipolar energy. c) Result of simulation when external magnetic field $\vec{B}_{\text{ext}}$ is applied. d) Result of the simulation when anistoropy with easy axis in vertical direction is added. With kind approval of the author adapted from [13].

1.2. Ferromagnetism

Materials which show spontaneous parallel order of the adjacent spins are called ferromagnetic (in te following denoted as FM) and as it was mentioned in subsection 1.1.1, they have a positive exchange constant J. Typical ferromagnetic materials are d-elements as Fe, Ni and Co. Ferromagnets exhibit non-zero spontaneous magnetization even when no field is applied. [14] The response of the ferromagnet to the applied magnetic field is not linear, as in the case of diamagnets and paramagnets. This behavior is described by a hysteresis loop. When all the magnetic moments are aligned in the direction of external field, there is no more contribution to the total magnetization by the increase of the external magnetic field. This maximal magnetization is called the saturation magnetization M_S and it is a basic characteristic of material. This parameter can be measured for example by Vibrating Sample Magnetometry and a typical value for Fe is around $\approx 1700\,\text{kA/m}$ [14].

1.2.1. Stoner-Wohlfarth model

The origin of the hysteresis loop could be explained by the Stoner-Wohlfarth model. Consider a system with uniaxial anisotropy K_u, with an easy axis along $\vartheta_{uni} = 0$ and with

uniform magnetization with magnitude M_S in a general direction ϑ. Magnetic field $\vec{H}_{\text{ext}}$ is applied in the direction ϑ_H. [15] Such system is described by the total energy $\mathcal{E}_{\text{total}}$

$$\mathcal{E}_{\text{total}} = \mathcal{K} \sin^2 \vartheta - \mu_0 H_{\text{ext}} \mathcal{M} \cos(\vartheta - \vartheta_H)\,, \tag{1.7}$$

where the anisotropy energy is $\mathcal{K} = K_u V$ and the magnetic moment $\mathcal{M} = M_S V$. It is obvious that $\vartheta - \vartheta_H$ is the angle between the external magnetic field $\vec{H}_{\text{ext}}$ and the magnetic moment $\vec{\mathcal{M}}$. Dividing the equation (1.7) by $\mathcal{K}$ and defining the effective anisotropy magnetic field strength as $H_a \equiv 2K_u/\mu_0 M_S$ will lead to

$$\frac{\mathcal{E}_{\text{total}}}{\mathcal{K}} = \sin^2 \vartheta - 2\frac{H_{\text{ext}}}{H_a} \cos(\vartheta - \vartheta_H). \tag{1.8}$$

For simplicity we defne a dimensionless energy variable as $e \equiv \mathcal{E}_{\text{total}}/\mathcal{K}$ and new dimensionless magnetic field variable as $h \equiv H_{\text{ext}}/H_a$. This leads to

$$e = \sin^2 \vartheta - 2h \cos(\vartheta - \vartheta_H) \tag{1.9}$$

The stable state is given by the derivative of the energy $\mathrm{d}e/\mathrm{d}\vartheta = 0$ and $\mathrm{d}^2e/\mathrm{d}\vartheta^2 > 0$. The direction of the magnetic moment (represented by ϑ) as a response to external magnetic field application will be complex and as h rises, for $h \gg 1$ the system behaves more as "only Zeeman-like" and the direction of the magnetic moment $\vartheta \to \vartheta_H$. On the other hand, as $h \to 0$, the leading contribution comes from the uniaxial anisotropy energy. According to this model, the system response to the applied magnetic field results in hysteresis and specific dependency on the direction of applied field, which is shown in Figure 1.3 for different angles between the easy axis and the applied field. Two most important cases

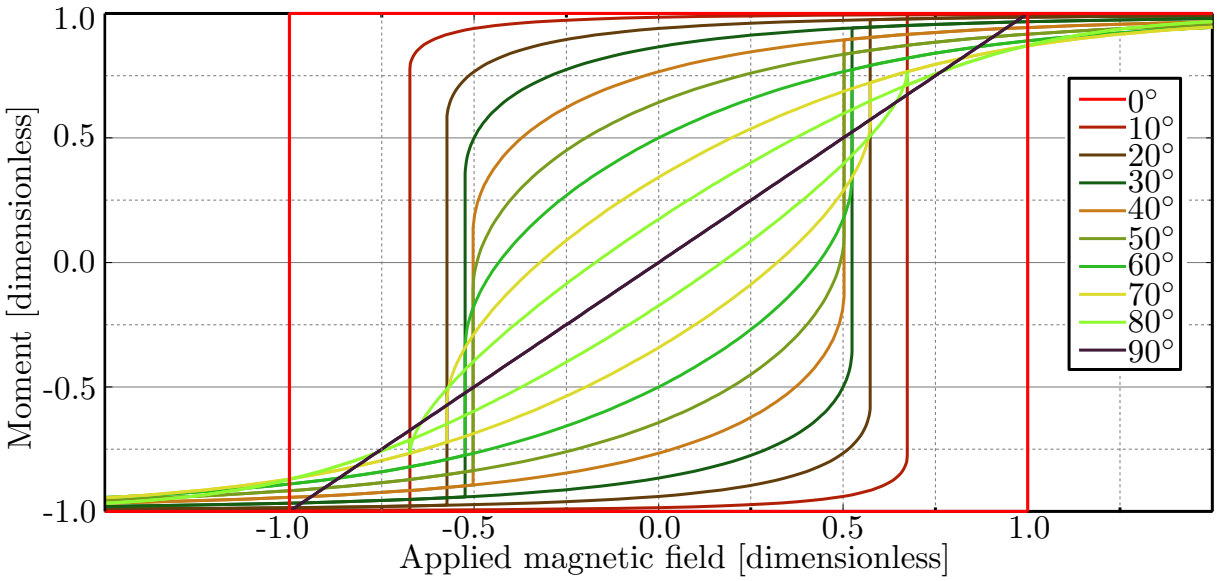

Figure 1.3: Graph of projection of magnetic moment to the direction of field versus magnitude of applied magnetic field. Different colors of curves correspond to the different directions of applied magnetic field – 0° represents the direction of easy axis and 90° stands for the hard axis. Adapted from [15].

can be distinguished. First, when the magnetic field is applied in the easy axis direction (0°) and second, when the field is applied in the hard axis direction (90°). The first case, when the magnetic field is applied in the easy axis direction, leads to a rectangular

hysteresis loops where the coercive field is equal to the effective anisotropy field strength $H_c = H_a$. In this case, the applied magnetic field has to overcome the anisotropy field and then abrupt magnetization reversal occurs. On the other hand, when the magnetic field is applied in the hard axis direction, the magnetic moments tend to follow proportionally to the magnitude of the applied magnetic field. As the magnitude increases to the effective anisotropy field strength, the magnetic moment is fully oriented in the direction of the applied magnetic field.

It shold be noted that the Stoner-Wohlfarth model is described only by the Zeeman and anisotropy energy terms, but in a real material the demagnetizing energy needs to be taken intp account. Despite this fact the Stoner-Wohlfarth gives a good first approximation for computation of the uniaxial anisotropy from hysteresis loops.

1.3. Antiferromagnetism

An other of materials showing spontaneous magnetic order are antiferromagnetic (AF in the following) materials. Antiferromagnetic materials have a negative exchange stiffness constant. AF materials appear non-magnetic on the outside, even though they are magnetically ordered. The magnetic lattice consists of two antiparallel oriented sublattices, which in sum give zero net magnetization, as shown in Figure 1.4.

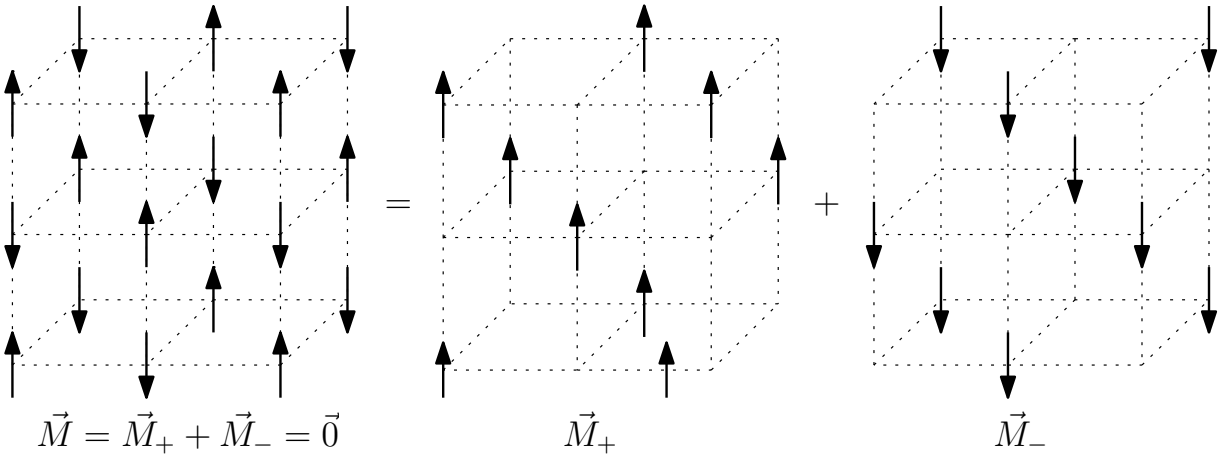

Figure 1.4: Antiferromagnetic lattice consists of two antiparallel oriented sublattices. The vector sum of these two sublattices gives zero net magnetization and "non-magnetical-like" behavior on the outside.

Typical antiferromagnets are elements like chromium and manganese [16], oxides of ferromagnetic materials (FeO, CoO) or other compounds (Cr_2O_3, MnF_2) [10]. The most relevant material for this work is equiatomic[5] alloy of Iron-Rhodium (FeRh), which is typically ordered antiferromagnetically at room temperature. Its properties are discussed in detail in chapter 2.

The behavior of an antiferromagnetic system upon application of external magnetic field strongly depends on the direction of applied field. In case the magnetic field is applied perpendicular to the axis of the antiferromagne (Figure 1.5a), it causes a tilt of the two magnetization sublattices towards the direction of the applied field. The response is linear with the magnitude of the applied magnetic field. This leads to constant magnetic

[5]Equiatomic means that the atomic concentration of Fe and Rh in the alloy is equal

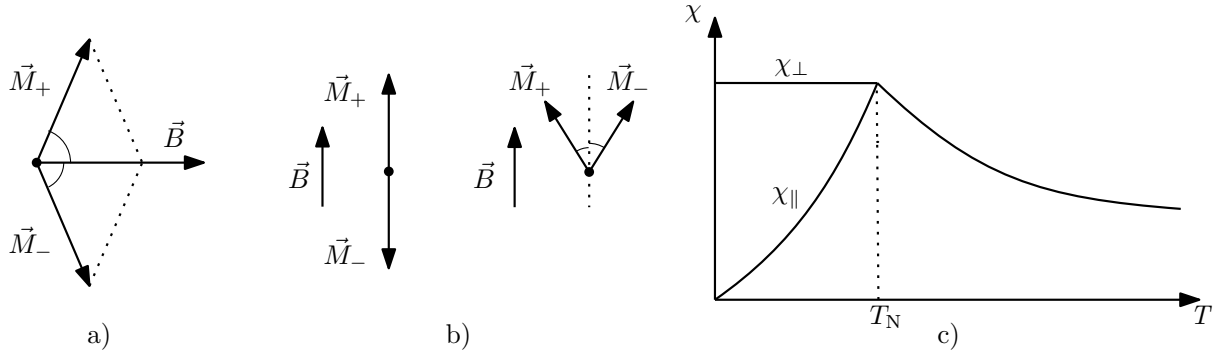

Figure 1.5: Figure of two different ways of applying a magnetic field to the antiferomagnetic material with vertical spin axis and corresponding graph of magnetic susceptibility vs temperature. a) Magnetic field applied to the perpendicular direction causes small tilt. b) Magnetic field applied parallel to the axis of antiferromagnetic material. For small magnetic field, a material remain the same. For higher magnetic field, a spin-flop transition occurs. c) Graph of magnetic susceptibility of antiferromagnetic material versus temperature. Adapted from [10].

susceptibility $\chi_\perp$ below the criticat temperature T_N at which the material transforms from antiferromagnetic to paramagnetic (Figure 1.5c). Above this so-called Néel temperature[6] T_N the magnetic order is destroyed by thermal fluctuations.

Different situation occurs when the magnetic field is applied parallel to the magnetization direction (Figure 1.5b). When the field is applied, Zeeman energy connected to M_+ is minimal, on the other hand, the energy connected to M_- is maximal in its metastable state. So for the small applied magnetic field and $T = 0\,\mathrm{K}$ the material stays antiferromagnetic. Under some critical magnitude of the magnetic field, the system will phase transform to the more favorable spin-flop phase. As the temperature rises $T \to T_\mathrm{N}$, the magnetic susceptibility for the parallel orientation goes $\chi_\parallel \to \chi_\perp$. [10]

There are several possibilities for aligning magnetic moments of single atoms in a lattice to obtain antiferromagnetic order. Four different possibilities of antiferromagnetic order in simple cubic crystal lattice are shown in Figure 1.6. The most common type of order is the G type, because of its minimal exchange energy.

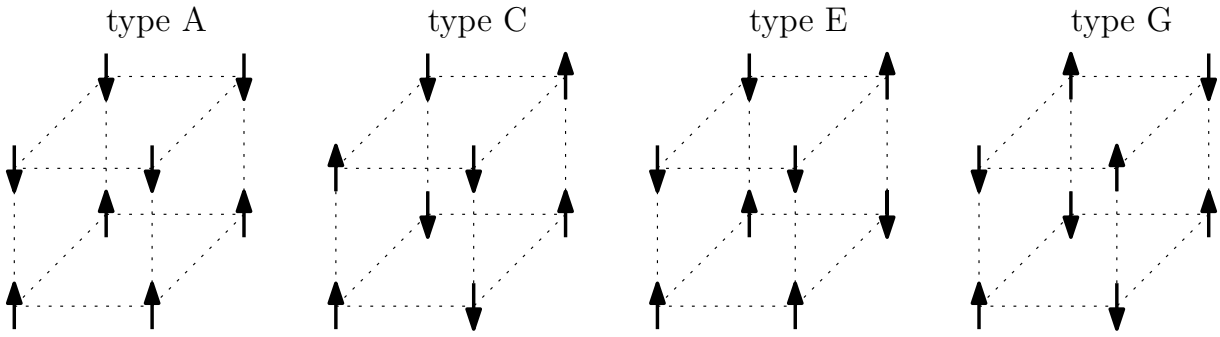

Figure 1.6: Four different possibilities how to align magnetic moments of single atoms to obtain antiferromagnetic order in simple cubic crystal lattice.

[6] In ferromagnetic materials the critical temperature is called the Curie temperature T_C

1.4. Phase transitions

Several different phase transitions may occur in a magnetic material. Basically, they are divided into two types – with and without the presence of latent heat. The phase transition from an ordered state (ferromagnetic or antiferromagnetic) to a disordered more symmetric (paramagnetic) state was already mentioned in section 1.3. From the thermodynamic point of view, this phase transition is a second-order phase transition, for which a continuous change of one phase into the other is observed at the critical temperature. Because of the continuity at the critical temperature, no latent heat is needed. In magnetism, the classical example is the FM to paramagnetic transition schematically shown in Figure 1.7b, accompanied by an increase of symmetry.

1.4.1. First order phase transition

Phase transitions with the presence of latent heat are called first-order phase transitions. Latent heat is connected to the discontinuities in thermodynamic quantities such as the entropy and the mass density during the phase transition. This transition is sometimes called abrupt phase transition. The most important property is the mutual coexistence of the phases, which enables the observation of the phase transition process by imaging the nucleation and growth of phase domains. [17, 18] In magnetism, the phase transition

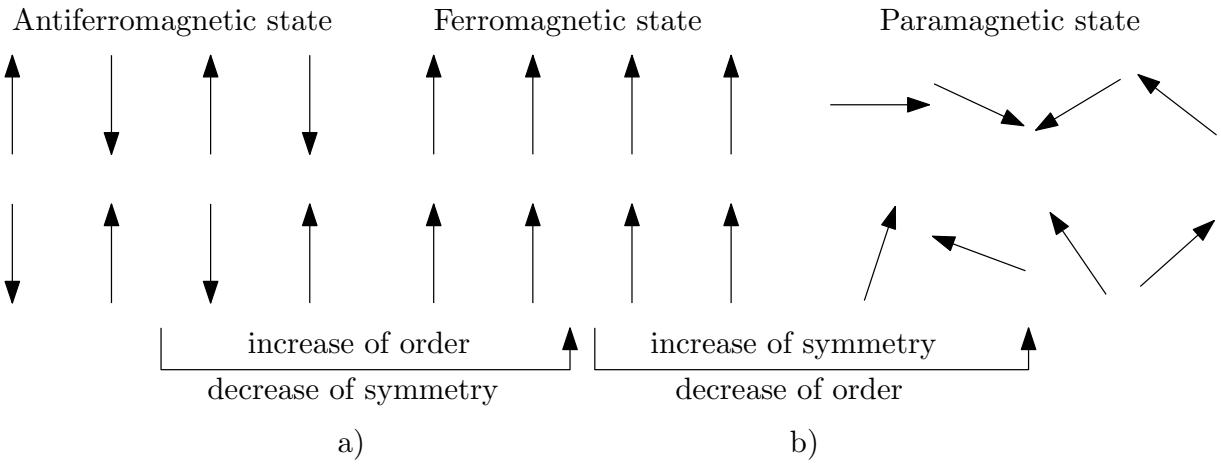

Figure 1.7: Scheme of the phase transitions between different the magnetic orders. a) First order phase transition from Antiferromagnetic state to Ferromagnetic state accompanied by increase of order and decreasing symmetry. Infinite AF lattice remains same under rotation by π and 2π while FM lattice only by rotation by 2π. b) Second order phase transition from Ferromagnetic state to Paramagnetic state indicating the increase of symmetry (the system remains same under any rotation) and decrease of order.

from AF to FM (schematically shown in Figure 1.7a) is accompanied by an increase of order, one of the order parameters being magnetization $|M| = 0 \rightarrow \left|\vec{M}\right| = \left|\vec{M}_+\right| + \left|\vec{M}_-\right|$. The order is always the consequence of broken symmetry [10]. While antiferromagnetic order is identical under rotation by π and 2π, the ferromagnetic order is identical only by rotation of 2π.

1.4.2. Stable and metastable state

In thermodynamics, the stable phase has to fulfill the Gibbs-Duhem stability criterion

$$\Delta U + p\Delta V - T\Delta S \geq 0, \tag{1.10}$$

where Δ stands for the variations of the quantities as internal energy U, entropy S and volume V, pressure p and temperature T. [18] The stable state is described with a minimum of thermodynamic potentials free energy F, free enthalpy or Gibbs energy G, Helmholtz free energy H, internal energy, and by a maximum of entropy. This criterion is used to find equilibrium conditions, but is insufficient for explanation why water cooled under 0 °C does not abruptly freeze and stays in the liquid phase called the supercooled liquid state. In order to distinguish between the three equilibrium states, the variations ΔS in terms of Taylor serie are typically introduced:

$$\Delta S = \delta S + \frac{\delta^2 S}{2!} + \frac{\delta^3 S}{3!} + \frac{\delta^4 S}{4!} + \ldots, \tag{1.11}$$

where δS, $\delta^2 S$, $\delta^3 S$, $\delta^4 S$ are differentials with respect to the state variables. [18]

- **Stable equilibrium** fulfills the condition of maximal entropy $\delta S = 0$ and $\delta^2 S < 0$ and all other differentials $\delta^3 S$,$\delta^4 S, \ldots < 0$.
- **Metastable equilibrium** also satisfies the condition of maximal entropy $\delta S = = 0$ and $\delta^2 S < 0$, but the condition $\Delta S < 0$ can be violated for some certain perturbation $\delta^3 S$,$\delta^4 S, \ldots > 0$.
- **Unstable equilibrium** does not meet the condition $\delta^2 S > 0$.

This is illustrated in Figure 1.8, which shows the stability region for a rectangle with an aspect ratio b/a. The stable equilibrium state corresponds to the minimum of potential

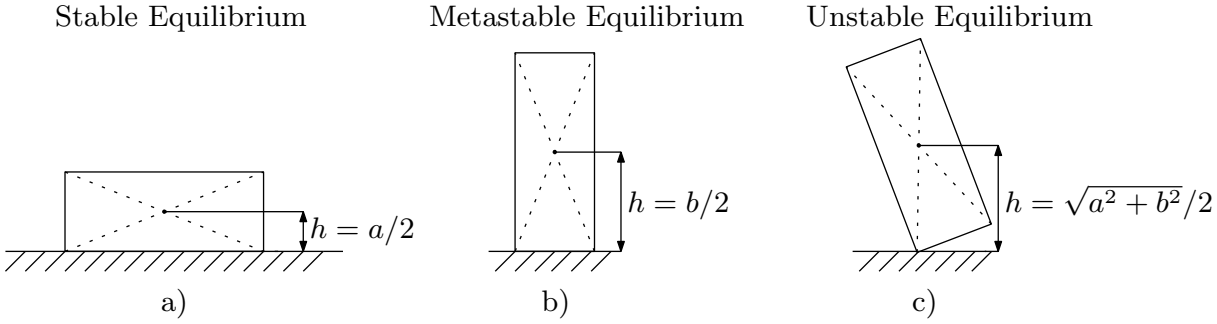

Figure 1.8: Illustration of three possible equilibriums. a) Stable equilibrium connected to the global minimum of potential energy. b) Metastable state equilibrium turned into an unstable by small perturbation $\Delta E = mg(b/2 - \sqrt{a^2 + b^2}/2)$. c) Unstable equilibrium, system tends to get to the stable or metastable equilibrium.

energy, as is shown in Figure 1.8a. Figure 1.8b shows the metastable equilibrium and when an acting force provides energy $\Delta E = mg(b/2 - \sqrt{a^2 + b^2}/2)$ the metastable equilibrium changes into an unstable equilibrium, shown in Figure 1.8c.

A better example of metastability is supercooled water which needs to be thermally or mechanical activated to turn to ice. [19] A common example of a material with unstable equilibrium is glass. [18]

1.4.3. Critical exponents

Second order phase transitions proceed through the so-called critical point. In the classical example of a second order phase transition, the transition from FM to the paramagnetic state, the critical point is called the Curie temperature. In the vicinity of the critical point the thermodynamic quantities obey a power law, where $X \propto (T_C - T)^x$, where x is so-called critical exponentpoint. Critical phenomena have an universal character, which is common for all the second order phase transitions. [18] Using the mean-field theory approach of Landau theory of ferromagnetism [10] in which all the independent spins feel the same effective exchange field, the magnetization behaves in the vicinity of Curie temperature as $(T_C - T)^{1/2}$ and magnetic susceptibility as $\chi \propto (T - T_C)^{-1}$. This describes a model situation, the real experiments are showing that the thermodynamic quantities follows

$$\begin{aligned} \chi &\propto (T - T_C)^{-\gamma} \qquad T > T_C\,, \\ \xi &\propto (T - T_C)^{-\nu} \qquad T > T_C\,, \\ M &\propto (T_C - T)^{\beta} \qquad T < T_C\,, \\ M &\propto H^{1/\delta} \qquad T = T_C, \end{aligned} \tag{1.12}$$

where χ is magnetic susceptibility, ξ correlation length referring to the order range of interaction and β, γ, δ, ν are so-called critical exponents. Critical exponents are universal for the system and there is a scaling law describing their mutual relationships

$$\nu d = \beta(\delta + 1) = \gamma \frac{\delta + 1}{\delta - 1}, \tag{1.13}$$

where d is the dimensionality of the system.

2. Magnetic phase transition in FeRh

Iron-Rhodium is intensively studied world-wide since the discovery of its antiferromagnetic to ferromagnetic phase transition in 1939 by Fallot and Hocart [1]. The transition occurs close to the room temperature and can be tuned by doping, magnetic field or lattice strain. Material remains, but objectives and methods of observation changed during time – from investigation of bulk samples to thin layers and patterned nanostructures which reveals new phenomena and effects connected to the confinement

The purpose of this chapter is to highlight important properties of FeRh and effects during the phase transition which can influence the imaging of phase domains or the transport measurements of FeRh layers and patterned structures. More information can be found in detailed reviews [20] or in theses submitted by the members of the Nanomagnetism and Spintronics group at CEITEC BUT in the last years. [6, 7, 21, 22] A review of current imaging techniques and their results will be provided within this chapter, too.

2.1. Introduction to Iron-Rhodium

Iron-Rhodium is a binary alloy $Fe_{1-x}Rh_x$ where x is the atomic concentration of Rhodium. Only in a narrow interval of 48−54 % of Rhodium atomic concentration, the FeRh alloy exhibits a phase transition from the AF to FM state during heating. After further heating the FM phase transforms to the paramagnetic state. The complete binary phase diagram can be found in [23].

FeRh crystallizes into simple cubic crystal lattice with a two atomic base, the Fe atom sitting at the origin 000 and the Rh atom in the position $\frac{1}{2}\frac{1}{2}\frac{1}{2}$ known as CsCl structure. The crystal structure is depicted in Figure 2.1a. [20, 23] The crystal lattice parameter for the low-temperature AF phase of the equiatomic FeRh alloy is $\approx$ 0.2986 nm [24]. Magnetic structure in the AF phase is like simple cubic structure with bases Cu_2AlMn where Cu atoms corresponds to the Rh atoms with zero spin. Al an Mn atoms represent Fe atoms with antiparallel oriented spins. The magnetic moments of Fe in the AF phase is $\mu_{Fe} = 3.3\mu_B$, while in the FM phase it slightly decreases to $\mu_{Fe} = 3.2\mu_B$. The rhodium magnetic moment is zero in the AF phase, while in the FM phase a moment of $\mu_{Rh} = = 0.9\mu_B$ is induced. [25, 26] Magnetic moments magnitude and orientations for the AF and FM phases are schematically shown in Figure 2.2. The phase transition in FeRh from the AF to FM state is a first-order phase transition (more discussed in section 1.4.1) significant with mutual distinguishability of phases at the transition temperature and the need for latent heat to induce the phase transformation from the AF to FM. The phase transition is not only connected to the increase of magnetization, but is is also accompanied by the increase of lattice parameter by 1−2 %. That is why the, the phase transition in this material is termed as the magneto-elastic phase transition. [20, 27] The phase transition is also accompanied by a 50 % reduction in resistivity [5, 20] and a large

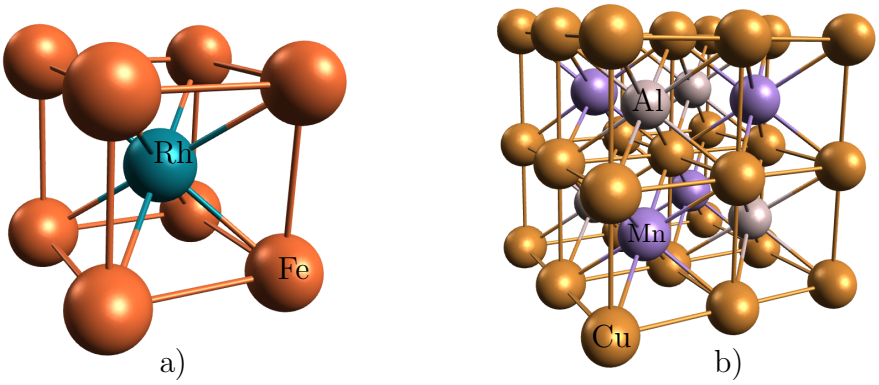

Figure 2.1: a) The crystal structure of FeRh corresponding to the structure of CsCl. b) The magnetic structure of antiferromagnetic phase corresponding to crystal of Cu_2AlMn where Cu atoms represents Rh. Al and Mn represent Fe atoms with antiparallel spins. The structure is then written as $Rh_2Fe\uparrow Fe\downarrow$. Adapted from [6, 23]

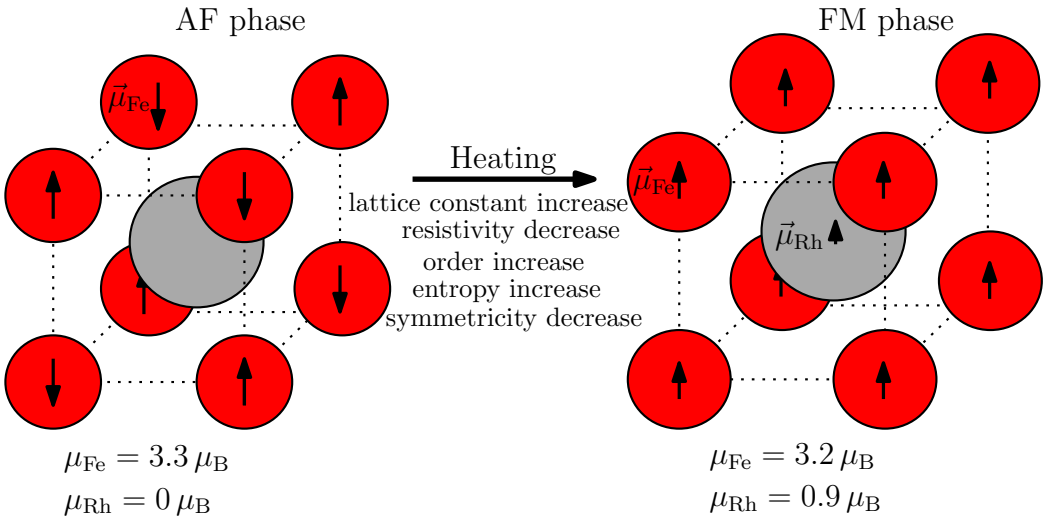

Figure 2.2: Phase transition in FeRh from the AF to FM state is accompanied with increase of magnetization (ordering), lattice constant and entropy but resistivity and symmetricity decrease. In the FM state magnetic moment is inducted on Rhodium. Red balls indicate Fe atoms and Gray balls indicate Rh atoms. Adapted from [6].

increase in entropy [27, 28] which makes the FM phase more temperature stable than AF phase [29] – giving the explanation of observed hysteresis loops between AF-FM and FM-AF phase transitions. The width of hysteresis is about 10 K [27] and is influenced by substrates and defect amounts (nucleation centers), terraces. C-axis sapphire $Al_2O_3(0001)$ or MgO(001) are often used as substrates. Thin films and structures used in this work are grown on MgO(001) substrate. [21, 22, 27] FeRh grows on MgO(001) rotated by 45°, which defines the easy axis of magnetic anisotropy in this direction (the second one in the perpendicular direction in the plane of the film).

Besides temperature, the phase transition in FeRh can be controlled by applying external magnetic field or pressure. In the case of magnetic field application, the transition temperature is reduced by a factor of $-8.3\,K/T$ for bulk FeRh [24] and by a factor of $-8\,K/T$ in the case of thin layer grown on MgO (001). [27] The shape of the hysteresis loop remains unchanged, it is only shifted in temperature.

The magnetic and structural transition are bound together. Applied pressure or compressive strain shrink the crystal lattice stabilizing the AF state. The measured factor is 4.336.3 K/kbar and varies for different atomic concentration of Rh. [30] The same dependence remains useful for thin layers, where the strain is caused by a lattice mismatch between FeRh and the substrate and for microstructures of FeRh, where the strain relaxation locally lowers the transition temperature on the edges of microstructure. [6, 7]

2.1.1. Spatial confinement effects

Unusual behavior is observed when the critical dimension of the FeRh system is reduced below the size of micron. In the experiment [5] which showed it for the first time, resistance versus temperature was measured for wires with different width: 1100 nm, 550 nm, 220 nm. The results of the measurement are presented in Figure 2.3. Measurement for a wire with width of 1100 nm shows expected continuous and symmetricc AF-FM and FM-AF transitions. Next measurement of wire with width 550 nm shows asymmetry between AF-FM and FM-AF transitions. Upon heating, the AF-FM transition stay continuous, while during the cooling, the FM-AF transition shows an avalanche-like behavior and the transition occurs in a single step. The measurement for wire with a width of 220 nm

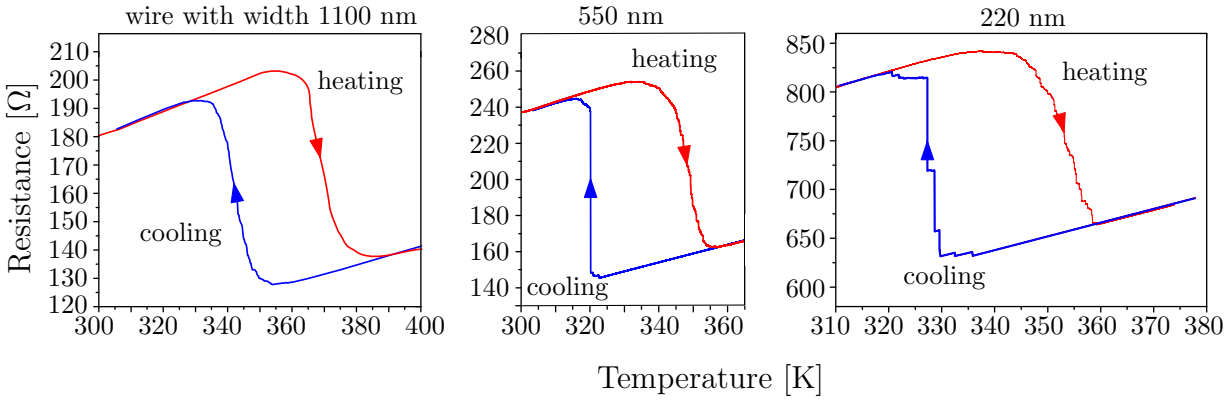

Figure 2.3: Resistance versus temperature measurement of wires with different widths 1100 nm, 550 nm and 220 nm showing the changed character of transition from continuous hysteresis to avalanche-like behavior when the critical dimension gets under one micron. The red curve indicates heating/AF-FM transition and The blue cooling/FM-AF transition. Adapted from [5].

highlights the fact that the transition does not have to proceed in one single step, but can proceed in several steps – although still abruptly.

The asymmetric behavior is explained by the different character of the AF and FM exchange interaction in the presence of defects. The FM ordering is not disrupted by small inhomogeneites in the structure such as defects in the crystal lattice and grain boundaries, while the domain sizes in the AF are determined by these inhomogeneites. This leads to different amounts of nucleation centers in the AF and FM phases, resulting in supercooling of the FM phase, where the number of nucleation centers is significantly lower. [5]

2.2. Imaging of phase transition

Electric transport measurement provides an average information of how the phase transition proceeds and helped to reveal asymmetry in phase transitions, however not giving information on how the domain appears at specific temperatures. Large systems as films or structure arrays can be observed by optical microscope with polarizers by MOKE method (Magneto Optical Kerr Effect). For smaller systems, scanning probe microscopy techniques – in particular Magnetic Force Microscopy (MFM) – can be used. The spatial resolution is around 50 nm, depending on the tip sharpness and shape.

MFM is the main used method in the experimental part of this thesis and is more discussed in the section 3.2. The next section reviews the use of MFM for the observation of the domain structure development and domain growth processes.

2.2.1. Imaging by MFM

MFM imaging can bring the information about the process of phase transition from a very small area, typically on the order of microns. Marekar et al. [31] investigated polcrystalline FeRh alloy which was prepared by melting Fe and Rh in an argon arc melting furnace. Figure 2.4 shows room-temperature measurement of sample which did not undergo phase transition. Figure 2.4a refers to the topography and Figure 2.4b shows the magnetic signal. For both presented measurement images, a line profiles along the lines A and B are shown. The phase coexistence on a sub-micron scale was showed and

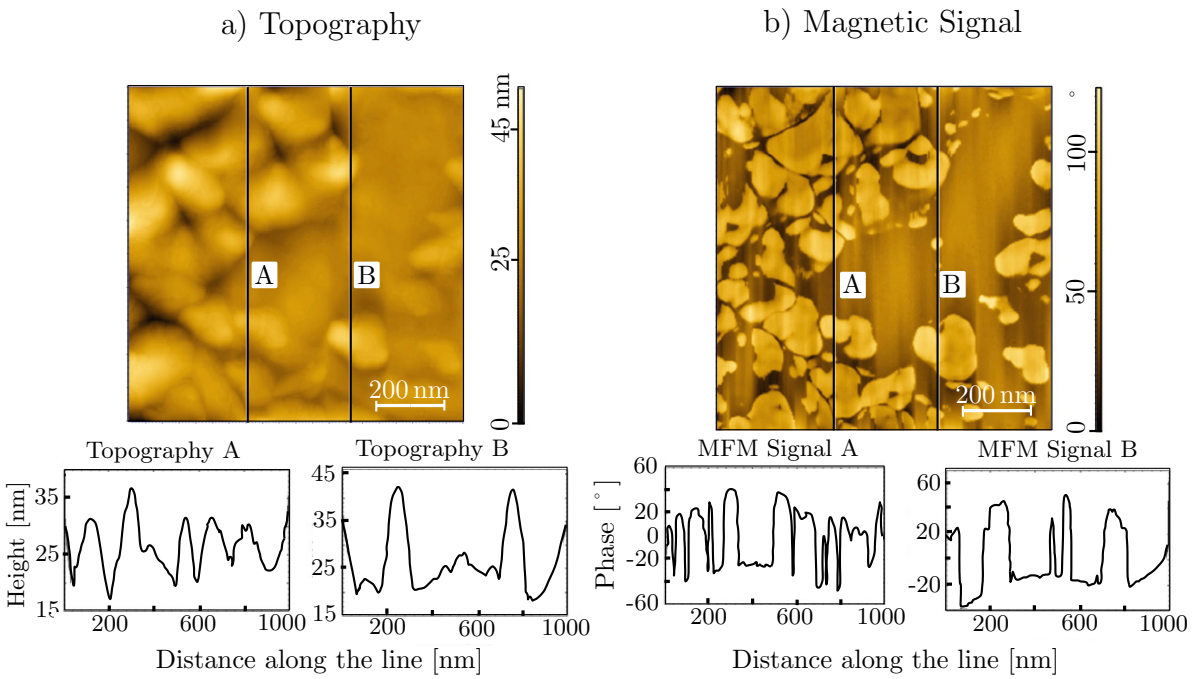

Figure 2.4: MFM surface room-temperature measurement of the bulk FeRh sample. a) Topography of the surface. b) Magnetic signal – phase. For both images are drawn profiles along the lines A and B with not processed (raw) data of the measurement. Adapted from [31].

through the time developments, the measurement showed a correlation between magnetic and the structural phase transition. [31]

Different strategy was chosen by Schánilec in his thesis [7], where the domain structure development at different temperatures was investigated. The researched structure was FeRh square of 3 μm size prepared from 50 nm thin FeRh layer grown on MgO (001). The cooling part of the measurement is shown in Figure 2.5a)-e) in temperature range

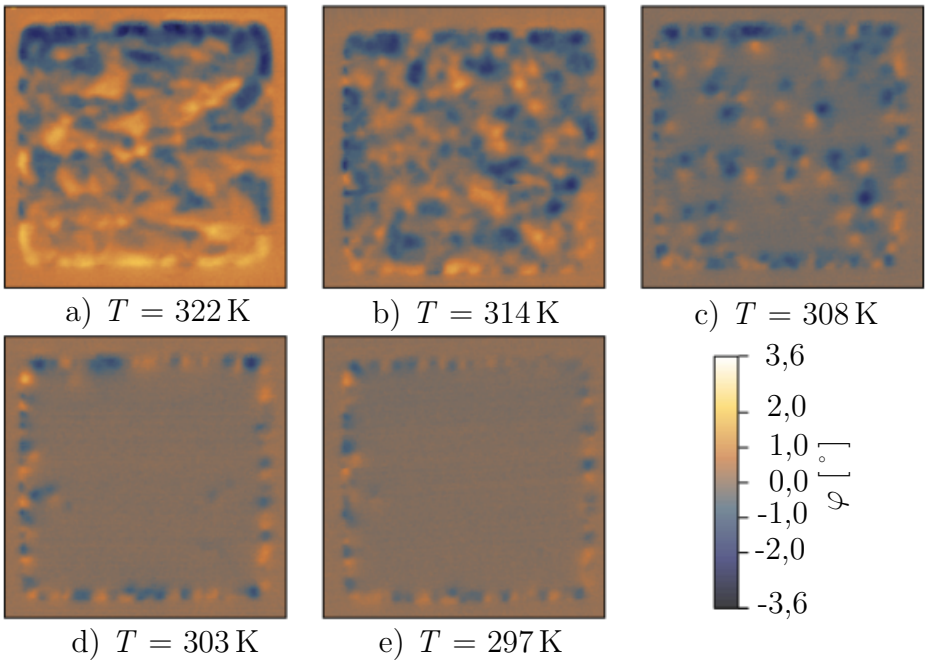

Figure 2.5: Temperature dependent MFM measurement of square structure pf 3 μm size patterned from a 50 nm thin FeRh layer in applied in-plane magnetic field with magnitude 29 mT. a)-e) MFM signal during cooling from 322 K to 297 K. Adapted from [7].

322−297 K and for better domain recognition, the nucleated FM domains were saturated to the direction of the applied static magnetic field with magnitude 29 mT. Measurements confirmed phase coexistence and indicated the presence of FM edges even at room temperature, caused by strain relaxation at the edges of the structure. Full measurement of cooling and heating loop on 3 μm square can be found in [7].

One year later in the author's bachelor's thesis[6], circular sub-microns structures and nanoislands with sizes of hundred nanometres were investigated. The MFM measurements were carried out in an out-of-plane magnetic field of 0.4 T to better visualize the phase domain boundaries. Analysis of the measured signal showed diferent behavior of the phase transition durin during cooling between 2 μm and 1 μm disc. The transition in the 2 μm disc was continuous, while in 1 μm disc an abrupt change occurred in integrated signal. The measurement suggested the avalanche-like character of the transition was inherent also in the magnetic order parameter. The observation of the nanoisland transition (Figure 2.6) showed an unexpected behavior – inverse transition from the FM to AF state during heating. Here the history of the phase transition is crucial. The sample was cooled to the room temperature in such way that some of the nanoislands stayed in a supercooled metastable state and through activation by heating they switched to the AF state, which was the stable state at the specific temperature. [6]

A complex study of the magnetic phase transition in several structures with length varying from 500 nm to 7 μm were done by Shao et al. [32] The observed material LPCMO ($La_{0.325}Pr_{0.3}Ca_{0.375}MnO_3$) undergoes the phase transition from a non-magnetic phase to

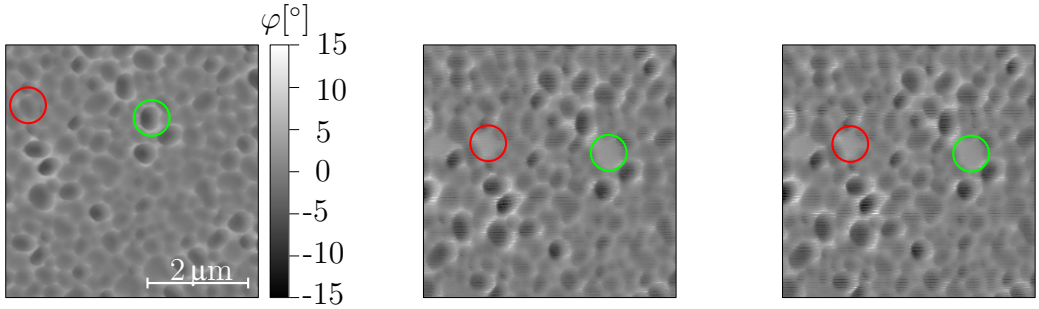

Figure 2.6: Temperature dependent MFM measurement of nanoislands in out-of-plane magnetic with field magnitude 0.4 T. Red and green circles indicates the unexpected transition from FM to AF state during heating. Adapted from [6].

FM at low temperatures. In Figure 2.7a the topography of measured discs is shown and in Figure 2.7b-d the MFM signal at temperatures of 10 K, 100 K, 180 K, respectively, is shown. The main finding of the work [32] is the existence of single-phase state when the spatial dimension is reduced to 500 nm.

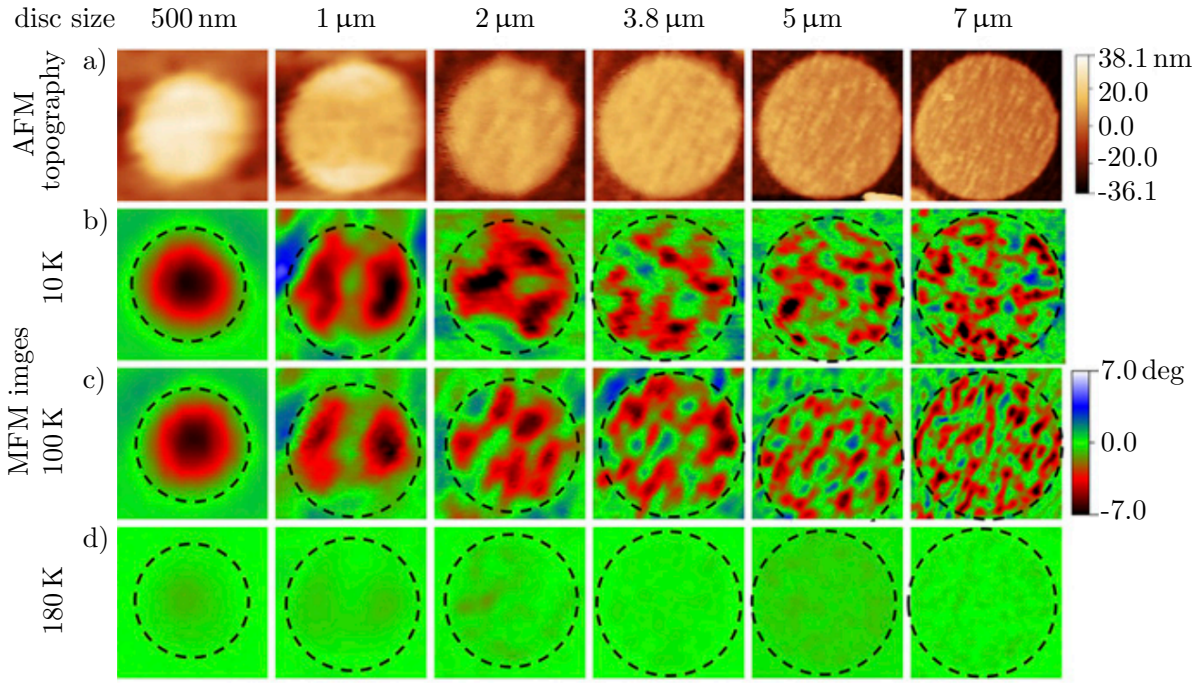

Figure 2.7: a) AFM topography images of LPCMO discs with sizes of 500 nm, 1 µm, 2 µm, 3.8 µm, 5 µm, 7 µm. b)-d) MFM images of domain structure at different temperatures 10 K, 100 K, 180 K, respectively. Dashed line indicates physical boundary of disc. Adapted from [32].

Phase domains, domain structure and processes during phase transition are not investigated solely by the MFM, other technoques are used for the research of this topic, such as MOKE [33] or by X-ray Magnetic Circular Dichroism (XMCD) [34, 35].

3. Experimental methods

This chapter provides important information, details and references to the methods of measurements, experimental set-ups, experimental conditions, sample preparation, and data analysis.

3.1. Preparations of the sample

Epitaxial films of equiatomic FeRh were grown on MgO (001) substrate by magnetron sputtering in the BESTEC[1] sputtering system. The substrates were pre-annealed at 720 K for 20 minutes for desorption of impurities and stabilization of the temperature before the deposition. The first four minutes of the depositions were performed at the same temperature and chamber pressure of 2.8×10^{-3} mbar, then during the deposition the temperature was raised to 870 K and held constant for the next four minutes. Then the temperature was raised to 1070 K and at this temperature, the deposition continued for additional twelve minutes. According to the deposition speed and the time of the deposition, thin films with thickness of 25–200 nm were prepared. The films were post-annealed at 1070 K for 45 minutes and subsequently coated with a 2 nm Pt layer which prevents film oxidation.

All created layers were characterized by Vibrating Sample Magnetometry using the Cryogenic[2] or Versalab[3] instruments to easily measure the development of the magnetization as a function of temperature. The FeRh films with an appropriate width of hysteresis and temperature of transition were then patterned into discs using a negative resist mask by electron beam lithography using TESCAN MIRA3[4].

The fabrication of the samples is not the objective of this work and author the is thankful to J. Hajduček, M. Horký, J. Liška and J. Arregi for providing the samples. More information about methods and experimental conditions of preparation can be found in [6, 22, 36].

3.2. Magnetic force microscopy

Images of the phase domain structure and its development were obtained by MFM. MFM is using similar tips to AFM, except for the MFM tips are coated with a magnetic material – the magnetic moment which interacts with the stray magnetic field created by the sample. For the imaging, the dynamic mode of measurement was used, where the

[1] www.bestec-berlin.de
[2] www.cryogenic.co.uk
[3] www.qdusa.com
[4] www.tescan.com

cantilever oscillates at frequencies close to the resonant frequency [37, 38] in the *MFM lift height* above the sample topography. The detected signal is a phase shift in oscillation which is proportional to the force gradient. Force is the gradient of Zeeman-like energy, hence the detected phase shift is proportional to the second derivative of magnetic stray field. Attractive forces correspond to positive phase shifts and repulsive forces to the negative ones. The measurement consists of two passes of the tip above the sample, first for acquiring topography and second for acquiring magnetic signal in the *MFM lift height*. [37, 38].

The principle of the MFM signal detection is shown in Figure 3.1. A laser spot illuminates the cantilever and from it the laser beam is reflected to the four element diode which converts the laser spot intensity to voltage in four independent segments. The difference in voltage from the upper two segments and the two bottom ones provides information about the deflection of the cantilever in the vertical direction, while the difference in voltage from the left two elements and right two elements provides information about deflection in the horizontal direction. This information is forwarded to the control electronics providing feedback. The signal is then recorded in the form of a phase shift or a frequency shift at a specific position on the surface. [38]

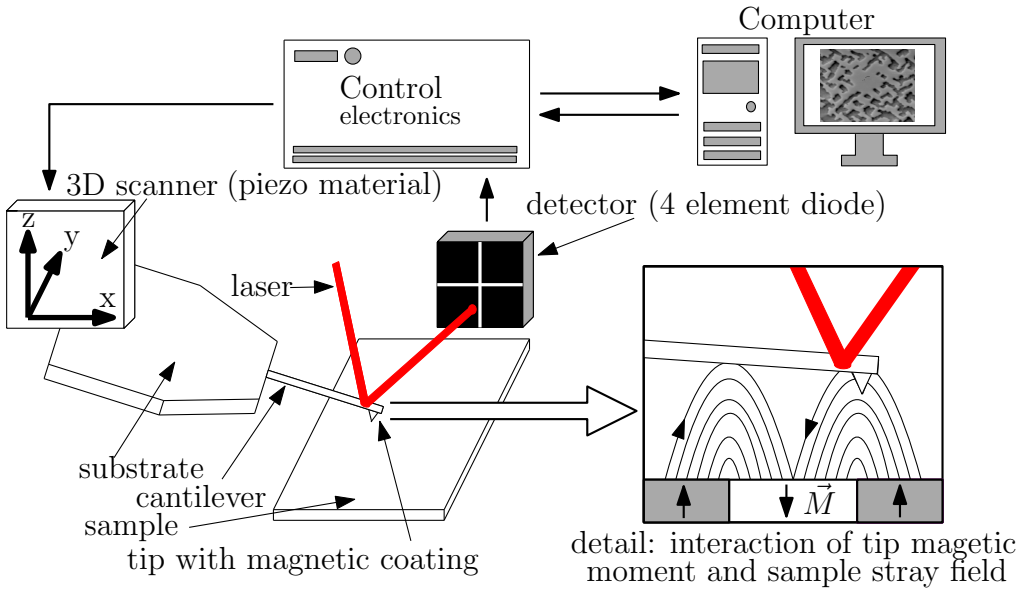

Figure 3.1: Illustration of MFM technique – principles of detection MFM signal. Adapted from [6, 38]

The typical resolution of MFM tips is 30 nm [39] and is linked with the maximum spatial frequency possible to be transferred by the instrument – also described by the Tip Transfer Function (TTF). The measured signal is then convolution of the Real Image with TTF. This is the basic concept for doconvolving mechanisms in reconstruction of real data from guessed or estimated TTF. Many publications were published on this topic, for instance [40] deals with the determination of TTF for MFM. Figure 3.2 shows how the real image is changed after the convolution leading to blurred edges. The tip can be damaged during the measurement or it can capture some impurities which change the TTF resulting in a change in the measurements output.

More information about MFM and AFM generally can be found in dedicated books [37, 38] or in the form of a review in any theses focused on MFM [41, 42].

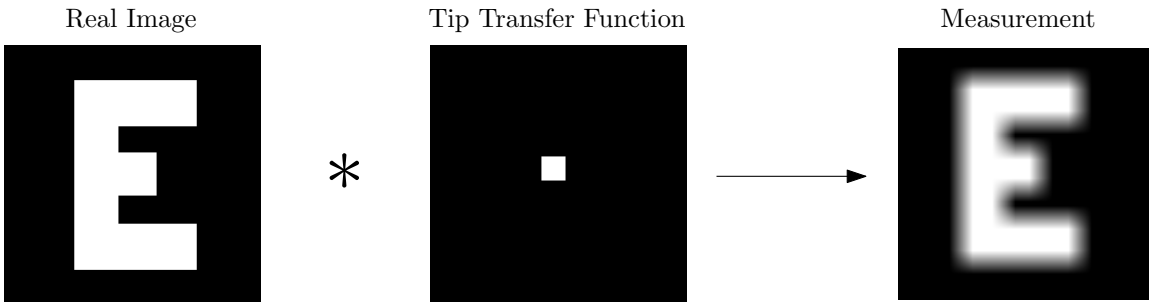

Figure 3.2: Image, how the real image could be changed after application of convolution leading to blurring of edges. Symbol * denotes convolution.

3.2.1. PeakForce Tapping Mode

The correct measurement of MFM signal relies on correct measurement of topography. In this work, the topography is measured by the PeakForce Tapping mode. [43] This mode is similar to the dynamic AFM mode with several differences. The main difference is that in the dynamic AFM mode, the tapping piezzo in the probe holder is excited by alternating voltage at a frequency close to the resonance frequency. However, in PeakForce Tapping mode, the z-piezzo is excited at frequencies 1 kHz or 10 kHz, decreasing the influence of magnetic field on the measurement of topography. During the modulation in z-axis, the tip experiences three significant different forces – the van der Waals attraction, repulsion and adhesive forces. When the peak-to-peak difference of force is higher than the *PeakForce Setpoint*, the z-piezzo is retracted and topography information is saved. [43]

3.2.2. Experimental setup for MFM

Imaging of the phase transition requires precise control of the sample temperature. For this purposes a temperature control stage compatible with the SPM instrument Bruker Dimension Icon[5] was used. More technical details can be found in [6]. In Figure 3.3, a simple scheme of the setup used for measurements is depicted. The setup consists

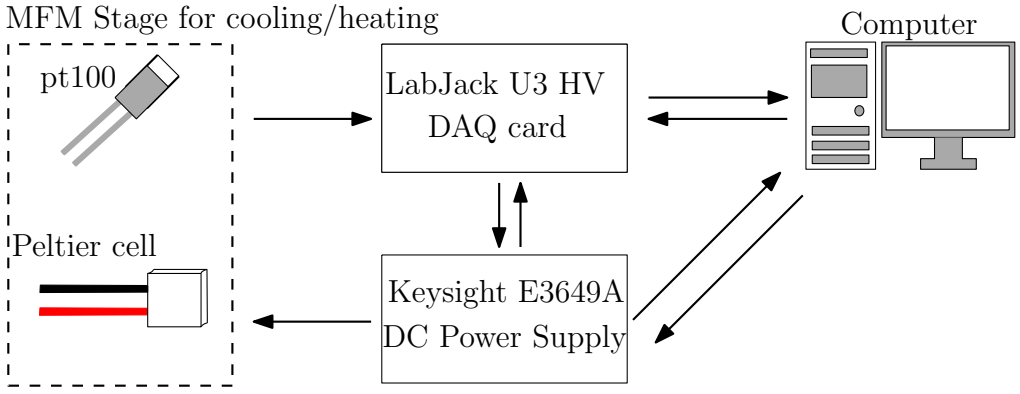

Figure 3.3: Scheme of MFM experimental setup for temperature control measurement.

of a heated stage with a temperature sensor pt100 and two active Dual-Stage Peltier cells. Peltier cells were used, because the voltage polarity allows to switch from sample heating to sample cooling. More about the function of Peltier cells is written in [7].

[5] www.bruker.com

The temperature is read through the Data Acquisition card LabJack U3HV[6] using the LABView[7] software. The Labjack is power supplied directly from the computer while the Peltier cells are power supplied by the Keytsight E3649A DC Power Supply[8]. Part of the LABView program consists of the PID regulation of the temperature with optional choice of individual PID parameters.

3.2.3. MFM Experimental conditions

The temperature-control setup works in an approximate temperature range of $260-383\,\mathrm{K}$ with temperature stability of $\pm 0.2\,\mathrm{K}$. Out-of-plane magnetic field with magnitude of $0.4\,\mathrm{T}$ is provided by a permanent magnet situated under the sample. MFM measurements were done by dynamic MFM using commercially available tips MESP[9] with CoCr magnetic coating . These tips have the nominal resonance frequency $75\,\mathrm{kHz}$, nominal stiffness $2.8\,\mathrm{N/m}$ and magnetic moment $1 \times 10^{-16}\,\mathrm{Am}^2$. The first pass topography was measured in the PeakForce Tapping mode with the z-modulation frequency of $1\,\mathrm{kHz}$. The *MFM lift* parameter was chosen in the range $80-120\,\mathrm{nm}$ above the sample topography. The *MFM lift height* parameter was kept constant for each set of measurements, in order to make the measurement outputs consistent. The *MFM lift height* will be specified for each set of measurements discussed in chapter 4. Impurities on the sample can introduce scars and errors in the measurement and thus the samples are cleaned in ultrasound with acetone and isopropanole prior to the measurement. The thermal contact between the sample and the temperature stage is improved by a double-sided copper tape. The copper tape is also used to fix the temperature sensor pt100 which is situated in the immediate vicinity to the measured sample.

3.3. Interpretation of MFM signal

MFM measurements is most often in literature and articles [6, 7, 31, 32, 38] interpreted in the form of an image. That is represented by matrix elements $\varphi_{i,j}$ which is scaled to some specific colour scale by choosing the minimum and maximum phase. Quantitative information from MFM measurements is partly based on methods from previous work [6]. There we gained absolute integrated signal where is the information is thresholded: "1" corresponds to the magnetic signal and "0" to non-magnetical background.

In this thesis we implemented a different approach based on he Height-Height Correlation Function (HHCF). [44–46] This function correlates squared heights difference of pixel pair as a function of their distance. The specific distance where the local order goes to long-distance order where the HHCF signal settles to a global roughness (height difference) value is denoted as the correlation length. This correlation length is a specific value for each temperature measurement and provides information about the average domain size. Both methods are discussed in the following sections.

Data were processed by scripts programmed in Python3 and MATLAB (included in the attachment). We have used Gwyddion software for SPM data processing Gwyddion [47] was used for the first approach to evaluate the HHCF.

[6] `www.labjack.com`
[7] `www.ni.com`
[8] `www.keysight.com`
[9] `www.brukerafmprobes.com`

3.3.1. Absolute integrated signal

Raw measurements contain a lot of incorrectly measured information, such as scars or additive noise. The magnitude of measurement phase in the scars could be ten times or more higher than typical values for the measured magnetic signal and needs to be suppressed. This is achieved by looking for a continuous area in the histogram of measured data. A typical histogram is shown in Figure 3.4 from raw data of 2 µm and 1 µm discs. Histograms are created for 256×256 values sorted to 250 intervals. [6] The histogram in

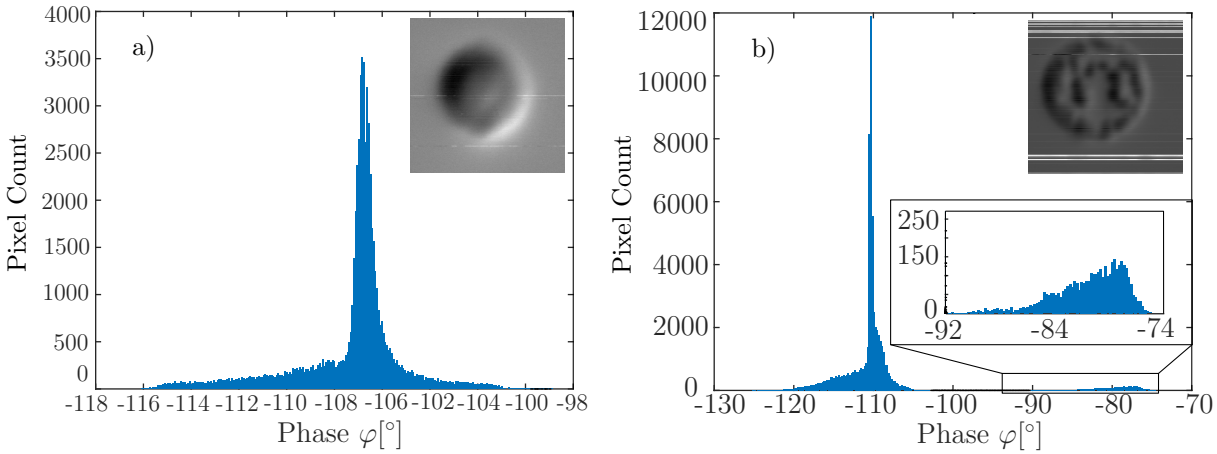

Figure 3.4: Histogram of raw data measurement of MFM signal. a) Histogram of measurement without scars. b) Histogram of measurement with big counts of scars. Adapted from [6]

Figure 3.4a shows measurement without scars. The phase shift of most pixels is continuously distributed around the maximum. However, Figure 3.4b shows a measurement with a high number of scars resulting in the division of one continuous histograms into two continuous areas. The first area looks similar to the histogram in Figure 3.4a referring to the pure data, the second area in Figure 3.4b refers to the scars. The scar reduction is done in two consecutive steps. Firstly, all the values outside of the first continuous area are substituted with a value of the median of the measurement. In case the image contains much more pixels of non-magnetic background than magnetic signal, the median of the image/measurement is a good approximation of the value of the non-magnetic background. Secondly, a median filter with 5 nearest neighbors is applied to all pixels in the measurement. [6]

The next step is to offset the pixel values of all measurements in such a way that the non-magnetic background is always 0. To visualize the measurement is needed to select uniform maximal and minimal values for color scaling.

The absolute integrated signal is then gained by thresholding the image into ”1” which corresponds to the magnetic signal and ”0” corresponding to non-magnetic background. The selection of a proper boundary for the threshold is discussed in [6]. This work uses a method with rigid boundary for all measurements in the set which is given by a mean of all boundaries with a given variance.

The whole procedure is schematically shown in Figure 3.5. The raw data in Figure 3.5a are shifted using the procedure described above to for them image in Figure 3.5b. The next step is the application of a median filter to get Figure 3.5c. The last step is to apply the thresold function for getting the absolute integrated signal image in Figure 3.5d.

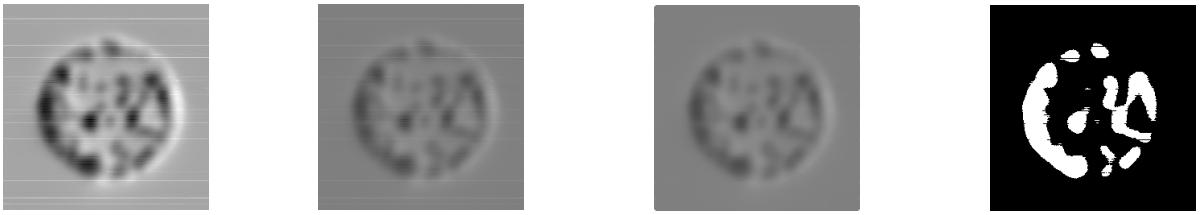

a) Raw Image b) Shifted to background c) Median filtering d) Threshold

Figure 3.5: Summarize of methods used during processing the raw measurement data. a) Raw Image b) All values shifted to value same for whole set of measurement. c) Median filtering with 5 nearest neighbors taking in account. d) Thresholded image where "1" corresponds to magnetic signal and "0" to non-magnetical background. [6]

This process was used only for a single structure disc MFM measurements and technically the computation was done in MATLAB (for more details see [6]). Evaluation of the MFM measurement for layers and arrays of discs was similar but with the difference that non-magnetic background is not always the median of pixel values but non-magnetic background was found by manual selecting using Span Selector in Python3.

3.3.2. Height-Height Correlation Function

The Height-Height Correlation Function is used in general SPM data processing and its vertical or horizontal variant is fully implemented in the program Gwyddion program [45]. A classic example is using of HHCF for estimating the average grain size [46] and roughness of the specimen. In this work it is used for estimating the correlation length of magnetic domains. HHCF is defined for an image/measurement matrix with elements $z_{i,j}$ with size $M \times N$ where M, N denote the number of rows and columns respectively as

$$H(m,n) = \frac{1}{(N-n)(M-m)} \sum_{l=1}^{N-n} \sum_{k=1}^{M-m} (z_{k+m,l+n} - z_{k,l})^2 \tag{3.1}$$

where $m,n = 0, 1\,2\,3, \ldots, 255$ and representing all the possible distances between two pixels in an image. Real distances between two pixels are then according to m,n given by

$$r_{m,n} = \sqrt{m^2 + n^2}\frac{L}{M} \tag{3.2}$$

where L is the real length of a scan size and M is the length in pixels. HHCF calculates the average square of difference $(z_{k+m,l+n} - z_{k,l})^2$ of all pixels with the distance $\sqrt{m^2+n^2}$. The example in Figure 3.6 for a 3×3 image shows all the possible combination of pixels to calculate $H(m,n)$. Note that with increasing m,n the number of all possible combinations given by $(N-n)(M-m)$ is decreasing. $H(0,0)$ is from definition in relationship 3.1 equal to zero.

HHCF is closely bound to the Auto Correlation Function (ACF) which is used in signal processing to find repeating patterns or identifying missing fundamental frequencies [48]. When the sum in the relation 3.1 is rewritten into two sums

$$\sum_{l=1}^{N-n} \sum_{k=1}^{M-m} (z_{k+m,l+n} - z_{k,l})^2 = \sum_{l=1}^{N-n} \sum_{k=1}^{M-m} z_{k+m,l+n}^2 + z_{k,l}^2 - 2 \underbrace{\sum_{l=1}^{N-n} \sum_{k=1}^{M-m} z_{k+m,l+n} z_{k,l}}_{\text{ACF}} . \tag{3.3}$$

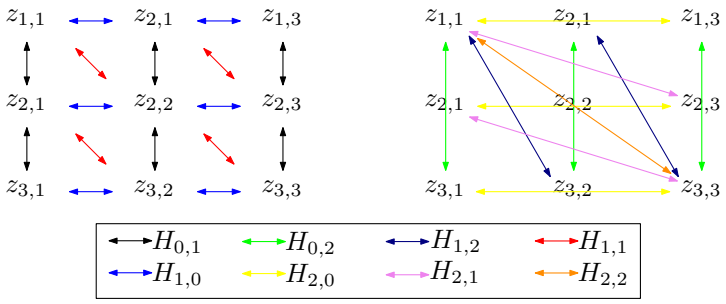

Figure 3.6: Scheme of terms used for calculation of each $H(m,n)$. Note that with increasing m,n the possible number of pixel combinations is decreasing.

The second sum is then (except factor $1/(N-n)(M-m)$) equal to the definition of discrete ACF. $H(m,n)$ could be represented as an image where $H(0,0)$ is situated in upper left corner. By choosing $n = 0$ we get one dimensional $H(m,0)$ which takes into account only the averages of row differences with the distance m along the fast scan axis. [45] The horizontal 1D HHCF calculation is given by

$$H(m,0) = H(m) = \frac{1}{(N)(M-m)} \sum_{l=1}^{N} \sum_{k=1}^{M-m} \left(z_{k+m,l} - z_{k,l}\right)^2 . \tag{3.4}$$

It is possible to obtain vertical 1D HHCF by choosing $m = 0$. Vertical and Horizontal 1D HHCF could be easily obtained by Gwyddion software by 1D statistical functions. Gwyddion software is used for basic characterization of HHCF properties. The model example is a $(512 \times 512)\,\mathrm{px}^2$ image with nine discs with a diameter of 50 px separated by 200 px. This model is divided into three color variants. Firstly, the model image with black background and two colored (gray and white) discs shown in Figure 3.7b. The next model image consists of white discs in black background, shown in Figure 3.7c. Figure 3.7d shows the model image shown in Figure 3.7b with additive noise. Images are represented by matrix elements where "0" belongs to the black color, "1" to the white color and "1/2" to the gray color. Figure 3.7a shows the 1D horizontal HHCF signal of image b),c),d) corresponding to red, blue and green, respectively. The interesting region for next processing is the interval 0A where the shape of the graph contains information about the correlation length and is crucial for later fitting. This is explained in the following paragraphs. At the B and C positions,a local minimum appears, which corresponds to mutual distances of discs: 200 px and 400 px. The additive noise shifts the HHCF signal to higher values, denoted by the D line.

HHCF analysis was done on MFM data measured on FeRh layers and FeRh structures with a diameter lower than 2 microns. The HHCF analysis on FeRh structures becomes more complex since the domain structure is confined by the finite size of the studied. At higher temperature when the FM domains are merged together, the disc starts to look as a homogeneous disc with no domain structure. This was confirmed by computing the $H(m,n)$ 2D HHCF function of real measurement data for 2 µm disc during cooling at 90 °C in Figures 3.8a,b and a model with white disc with the same diameter as used in the disc for real measurement and black background in Figure 3.8c,d. Size of the images is 3×3 µm. HHCF images in Figures 3.8a,d look similar, except for the image in Figure 3.8a which is modulated between the upper left corner and the maximum following the diameter of 2 µm corresponding to the real measurement disc diameter, while the image in Figure 3.8d is more continuous in the same area. As distance increases above 2 µm, the HHCF signal drops to zero.

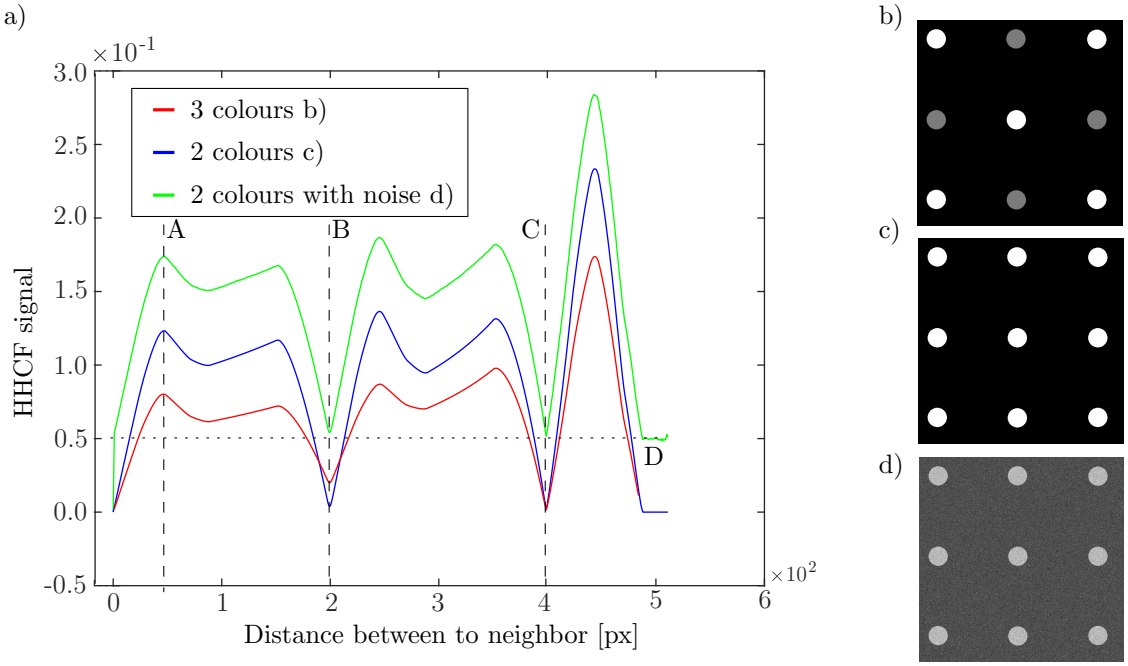

Figure 3.7: One dimensional HHCF function of different images. a) Graph of horizontal HHCF vs distance between neighboring pixels. Red colour represents image b) consists of 5 white discs and 4 gray on black background. Blue represents image c) with nine white discs on black background and green represents image d) which is noised image c). Interval 0A contains information about start of graph connected to correlation length. In B local minimum occurred when the distance between two pixels gets to 200 which is the distance of two discs. Minimum at C corresponds to distance 400 px which is the distance of two more distant discs. Line D symbolizes the shift of whole HHCF signal due to additive noise.

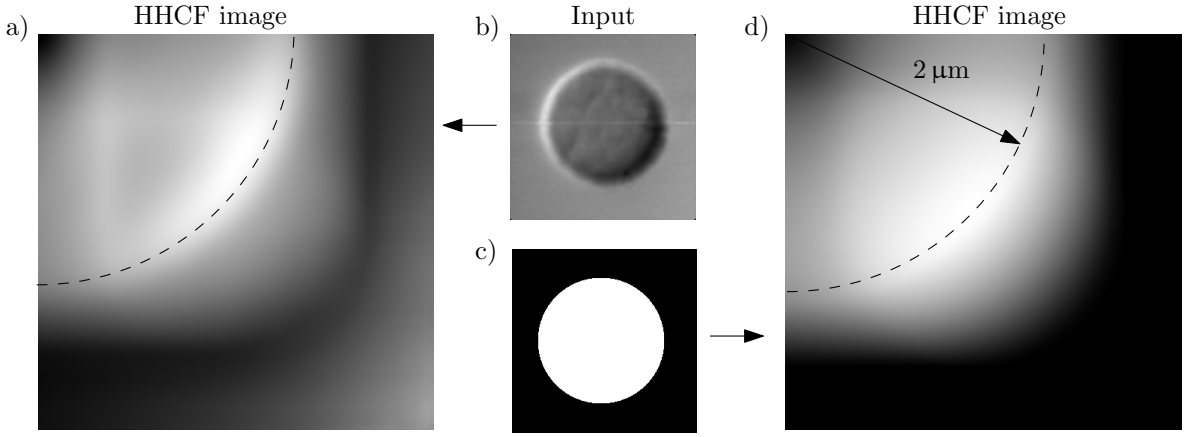

Figure 3.8: 2D HHCF images of discs. a) HHCF image computed from image b) real measurement of 2 µm during cooling at 90 °C. d) HHCF computed from c) which is a modeled image of same diameter as disc in image b).

The conclusion is that in the HHCF signal of measurement of a single structure there will always be the influence of the structure increasing at higher temperatures when the FM disc becomes homogeneous. This is the reason why later when the HHCF signal is fitted we take into account only values in the interval from zero to position of the first peak.

One way how to obtain the 1D HHCF was to use only the horizontal part ($H(m,0)$) or vertical part ($H(0,n)$) of $H(m,n)$. The second way is to sort the matrix elements $H(m,n)$ and $r(m,n)$ to one dimension as

$$r = \left(r_{0,0}, \frac{r_{1,0} + r_{0,1}}{2}, r_{1,1}, \frac{r_{2,0} + r_{0,2}}{2}, \ldots, r_{m,n} \right) \tag{3.5}$$

and

$$H = \left(H_{0,0}, \frac{H_{1,0} + H_{0,1}}{2}, H_{1,1}, \frac{H_{2,0} + H_{0,2}}{2}, \ldots, H_{m,n} \right) . \tag{3.6}$$

As $r_{m,n} = r_{n,m}$ are equal to the same distance, the corresponding HHCF signal for this distance is taken as the mean $(H_{m,n} + H_{n,m})/2$. This approach produces more information about the image and about the shape of HHCF signal than only the horizontal or vertical HHCF approach.

In the reports[44–46] the 1D HHCF signal vs distance r is fitted by the function

$$H(r) = 2\sigma^2 \left(1 - \exp\left(-\frac{r^\alpha}{\xi^\alpha} \right) \right) . \tag{3.7}$$

Single parameters from this fit estimate roughness σ (in our case "magnetic roughness" of magnetic signal), correlation length ξ after the HHCF signal stabilizes at global roughness, used for estimating average domain size (grain size) and parameter α describing the graph shape of the HHCF signal in interval close to 0. The fitting is shown in Figure 3.9 for the HHCF signal of two measurements of a thick FeRh layer at the temperature of 60 °C during heating and temperature 89 °C during cooling. The scan size is 11 µm on 256 px so the 1 px corresponds to ≈ 43 nm. In Figure 3.9a the system is deep in the AF state

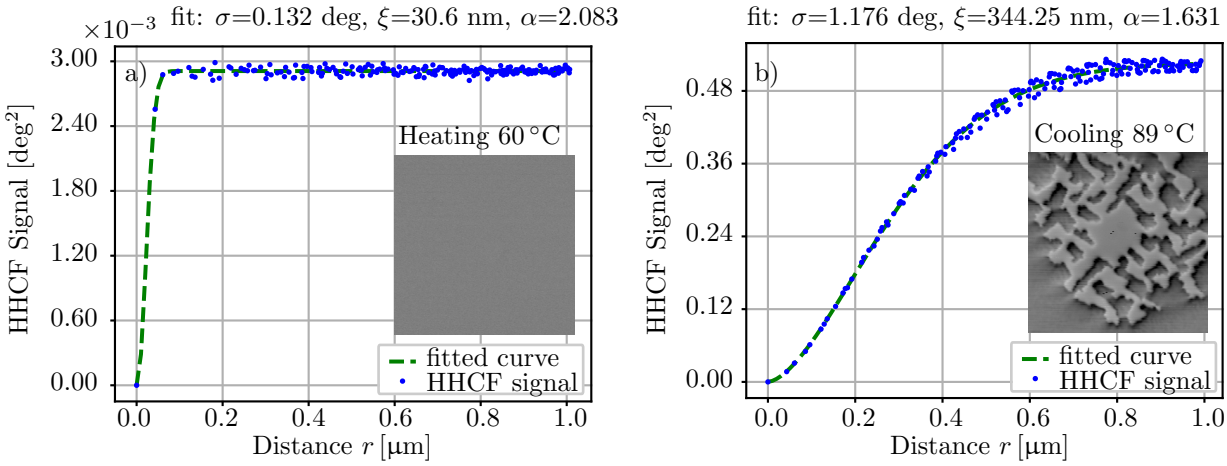

Figure 3.9: Two fitted HHCF signal vs distance r to estimate parameters as "magnetic roughness" σ, correlation length ξ and α influencing the shape of the graph. a) Fitting of HHCF signal for only noise measurement of FeRh layer at 60 °C during heating. b) Fitting for measurement of FeRh layer at 89 °C during cooling.

so no magnetic signal corresponding to FM domains was detected, only the noise of the measurement. Even this can be fitted and the resulted correlation length $\xi = 30.6$ nm which is close to the pixel size. Magnetic roughness parameter is $\sigma = 0.132°$ which is close to always estimated noise level of MFM images. In Figure 3.9b the system exhibits phase coexistence. The calculated HHCF signal is fitted by the above-mentioned formula

[44–46]. The resulted correlation length is $\xi = 344.25\,\text{nm}$ and magnetic roughness is $\sigma = 1.176\,°$.

The same method is used for all the images in the individual sets of measurements. The results of this processing method applied on measurements of FeRh structures and FeRh layers are discussed in separate chapter 4, dedicated to experimental results.

The calculation of the 2D HHCF was done in MATLAB. The non-linear curve fitting was done using Python3 with Span Selector function to select the interval from 0 to the first peak. Non-linear curve fitting provides a covariance matrix of fitted parameters from which the uncertainty of single parameter was estimated. All used scripts are available in the attachment.

3.4. Stochastic nucleation investigation

Nucleation of the phase transition of the supercooled FM state to AF state is stochastic. Hence, the probability that the phase transforming event occurs within time t, is given by Poisson distribution

$$P = 1 - e^{\frac{-t}{\tau}}\,, \tag{3.8}$$

where the τ is a time constant that signifies the mean nucleation time. The supercooled FM state needs to overcome an energy barrier of ΔE to phase transform to the AF state. The thermally activated process of overcoming the energy barrier is described by Arrhenius law, where the probability of overcoming the energy barrier at temperature T is described by [49]

$$\tau = \tau_0 e^{\frac{\Delta E}{kT}}\,, \tag{3.9}$$

where k is Boltzmann constant and $1/\tau_0$ characterizes the property of the system – the attempt frequency. The attempt frequency $1/\tau_0$ is often chosen in the range of $10^8 - 10^{12}\,\text{Hz}$, which is a typical value for most magnetization processes. [49, 50]

This approach will be followed to estimate the energy barrier between the supercooled FM state and the AF state, by measuring the probability that the supercooled FM state transforms within the time t.

3.4.1. Experimental set-up for stochastic nucleation investigation

The stochastic nucleation experiment will determine the mean nucleation time needed to trigger the transition from the supercooled FM state to AF state. The change of the state can be detected by a resistance change $\approx 50\,\%$. [20] The fact that the detection of phase transition is done using resistance measurement demands a special samples with lithographically fabricated contacts and a FeRh wire/element with a single abrupt change. The single steps of the measurement are:

- Heat the sample to its fully FM state.
- Cool the sample close above the transition temperature (the experiment is done for specific ΔT from the transition temperature) and turn on a timer.
- Record the time until the abrupt phase transition.
- Repeat as many times as possible to get enough statistics to determine the mean nucleation time for a given ΔT.

The measurement is done using a temperature holder already used in work [22]. The experimental setup is similar to the temperature control setup for MFM measurements

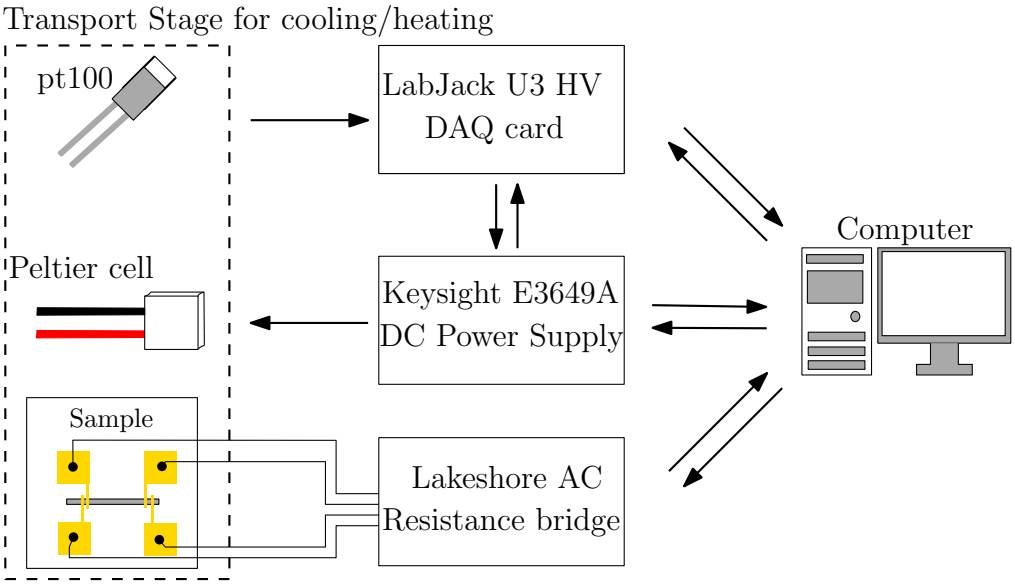

Figure 3.10: Scheme of experimental setup for stochastic nucleation investigation.

and the setup is shown in Figure 3.10. The only difference is addition of the Lakeshore[10] AC resistance bridge for measuring the resistance.

The whole experiment including heating, cooling, temperature reading and resistance reading is controlled by a program coded in LABView.

[10] `www.lakeshore.com`

4. Results

Qualitative and quantitative results of phase domain structure development during the magnetic phase transition are discussed in this chapter. Using MFM measurements we investigate the spatial confinement effects connected to the reduction of the film thickness and the effects emerging in patterned discs with different sizes. The supercooling effect is investigated by MFM measurements on arrays of discs and the nucleation stochasticity is recorded by transport measurement of a FeRh wire.

4.1. Samples overview

Several FeRh samples were fabricated via aforementioned methods (see section 3.1). Sample names, objectives of observation and thicknesses of the films before pattering are displayed in Table 4.1. The film thickness was measured by X-ray Reflection (XRR). *The MFM lift height* and the type of temperature measurement (heating vs. cooling) are included.

Table 4.1: Overview of the used samples and the details of the MFM measurements.

Sample	Object	Thickness [nm]	MFM lift [nm]	Measured
A26b	array of 500 nm discs	36	120	cooling only
A15	array of 700 nm discs	36	80	heating+cooling
	15 um disc	50	100	338 K cooling
	2 um disc	50	100	heating+cooling
X79b	1 um disc	50	100	heating+cooling
	700 nm disc	50	100	heating+cooling
	400 nm disc	50	100	heating+cooling
A21	film	36	80	heating+cooling
P17b	film	200	80	heating+cooling

4.1.1. Topography characterization

The topography measurement is an essential part of each MFM measurement and needs to be carried out correctly to provide accurate MFM measurement results. The topography was measured by the PeakForce Tapping mode using a $(256 \times 256)\,\mathrm{px}^2$ scan size.

Figure 4.1 depicts the topography measurement of various disc arrays. In figure 4.1a, the measurement of sample A15 with a 5×5 array of 700 nm discs is shown. This array is surrounded by a 300 nm wide frame. The addition of a frame which surrounds the arrays improves the stability of the measurement and significantly reduces the number of scars

and errors. The measured thickness of the structures is ≈ 80 nm, which is inconsistent with thickness measurement provided by XRR ≈ 36 nm. The thickness increase most likely occurred during the fabrication process and it corresponds to the undissolved resist. The thickness increase is common for all of the patterned structures. The measured area contains several non-magnetic impurities with thickness ≈ 300 nm. In Figure 4.1, the

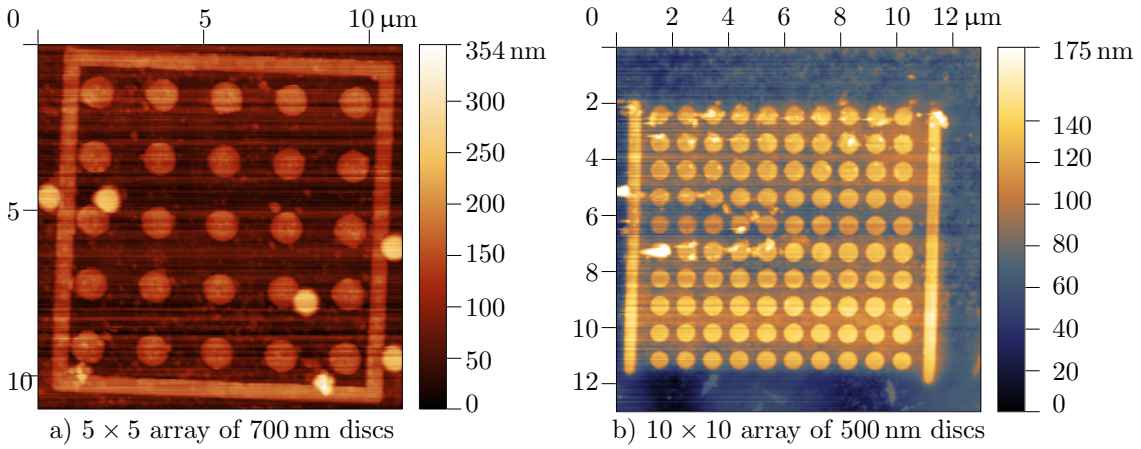

Figure 4.1: Topography measurement of disc arrays. a) Measurement of the A15 – a 5 × 5 array of 700 nm discs. b) Measurement of the A26b – a 10 × 10 array of 500 nm discs.

topography measurement of A26b is shown. The region of interest is a 10 × 10 array consisting of 500 nm discs. This array is supplemented by two vertical wires with the width of 500 nm improving the stability of the measurement in a better way than the frame displayed in 4.1a.

The topography measurements of the discs fabricated for investigation of the lateral confinement effect are shwom in the Figure 4.2. The topography of the discs with diameters 2 µm, 1 µm, 700 nm, 400 nm is shown in a), b), c) d), respectively. The width of the scan was kept the same and one image pixel corresponds to 3 µm/256 ≈ 11.7 nm.

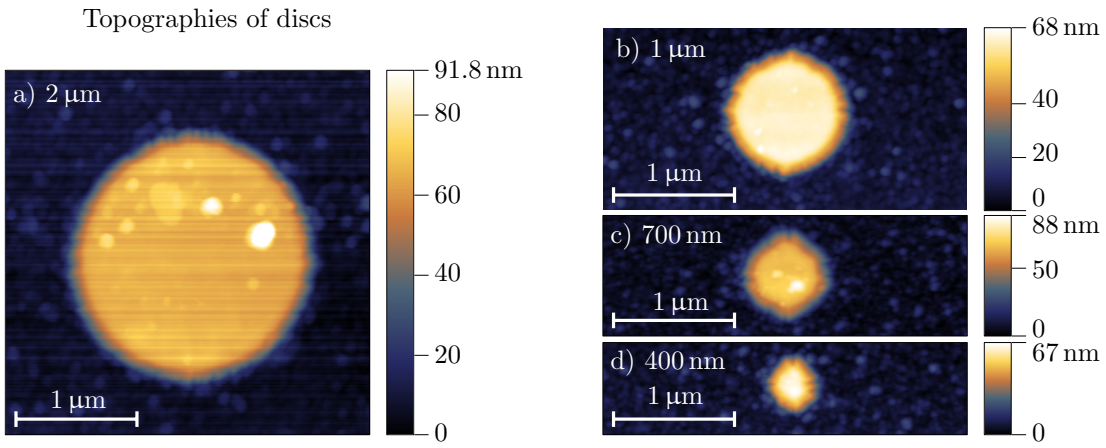

Figure 4.2: Topography measurements of single discs for the lateral confinement effects investigation. All the discs were present on the same sample – X79b. a) Topography measurement of the 2 µm disc. b) Topography measurement of the 1 µm disc. c) Topography measurement of the 700 nm disc. d) Topography measurement of the 400 nm disc.

The topography measurement of films on the sample P17b with the film thickness of 200 nm (Figure 4.3b) and on the sample A21 with the film thickness of 36 nm (Figure 4.3a) were done in an 11 µm wide scan window, resulting into 11 µm/256 ≈ 43 nm pixel size. The scanned areas were purposely centered around the defects to provide better orientation and a large-enough area with non-magnetic background, which is used for the correct color scaling of the images.

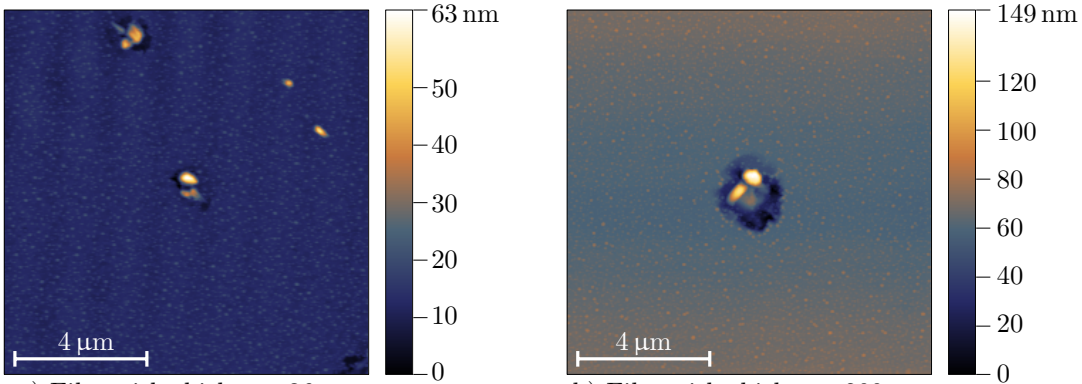

a) Film with thickness 36 nm

b) Film with thickness 200 nm

Figure 4.3: Topography measurement of the thin films. a) Topography measurement of the A21 with a film thickness of 36 nm. b)Topography measurement of the P17b with a film thickness of 200 nm. The scanned area was purposely placed in the middle of the defects to provide easy orientation and color scaling of the images.

4.2. Supercooling effect investigation

Supercooling and stochastic nucleation were observed qualitatively by measuring arrays of structures to provide larger statistics and quantitatively via transport measurement of FeRh wires. The results of these measurements are presented in the following subsections.

4.2.1. MFM imaging of stochastic nucleation

In the first case, the measurement of an array consisting of 700 nm discs and an array consisting of 500 nm discs is presented. These measurements were done with the *MFM lift height* parameter 80 nm and 100 nm, respectively. Both measurement sets were processed in the Gwyddion software by the following procedure. For each image in the measurement set, the mean value was zeroed[1] and the unified phase color scale representation for all images was set.

The measurements of the array of 700 nm discs were done for heating in the temperature range of 313–343 K, while the phase transition during cooling was observed in the temperature range of 343–302 K. Both measurements were done with a 1 K temperature step, in total 71 temperature steps. In Figure 4.4a-h, a part of the measurement during cooling is depicted for the temperature range of 313–302 K. Several different processes marked in Figure 4.4 occurred during the cooling. Firstly, the dashed green circle indicates a supercooled disc which did not phase transform within the measured temperature range. The solid yellow circle indicates phase transition through the continuous domains decay. The dashed-dotted red circle shows a supercooled state, which phase transforms

[1]Mean value in this case corresponds to the value of non-magnetic background

abruptly from a) 313 K to b) 312 K. Blue ellipse shows a supercooled rectangular element in the square frame phase transforming from g) 303 K to h) 302 K. These different pro-

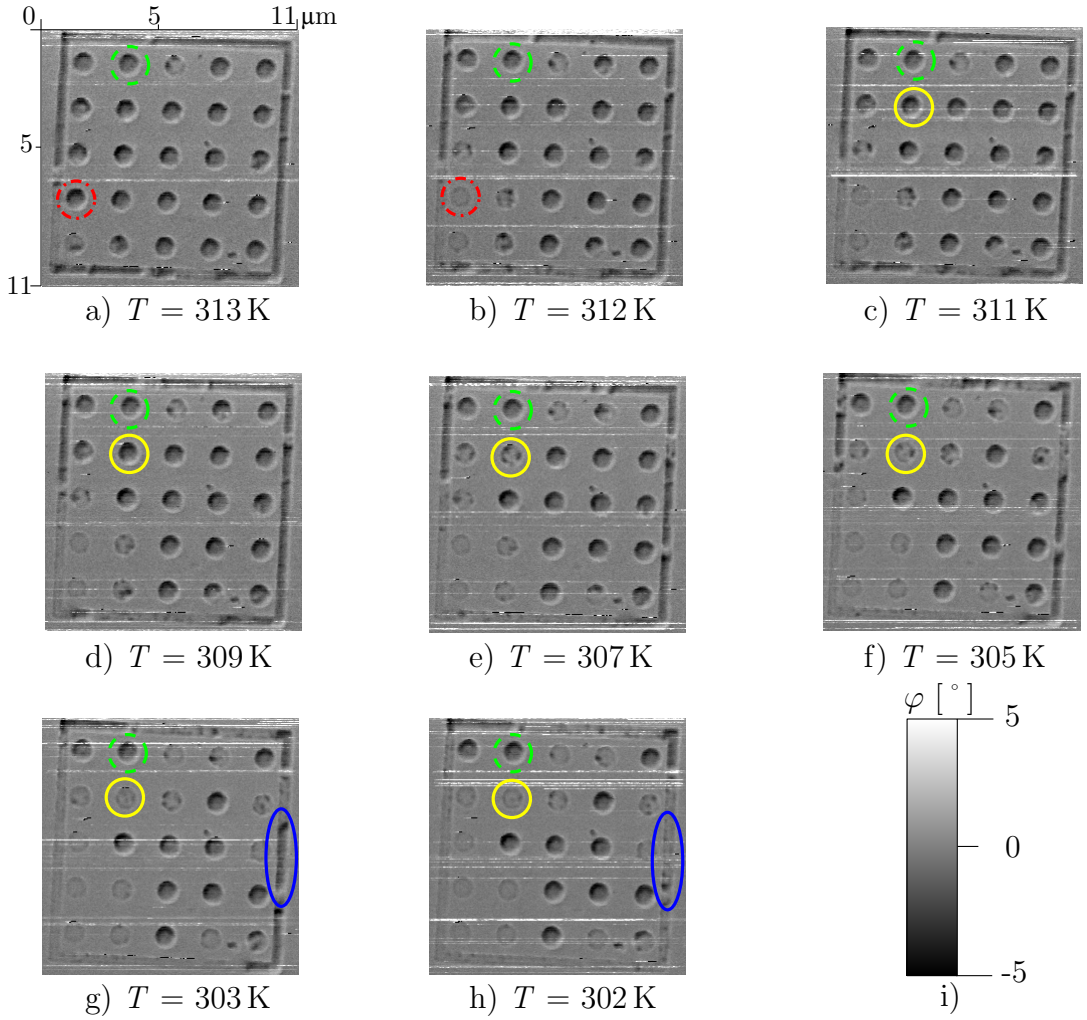

Figure 4.4: MFM measurement of the sample A15 with a 5×5 array consisting of 700 nm discs. In the images a)–h), the FM-AF phase transition is shown during the cooling in the temperature range of 313–302 K. Image i) shows the united phase color scale for all of the other images. The dashed green circle indicates supercooled disc which did not phase transform. The full yellow circle indicates phase transition through the continuous domains decay. The dashed-dotted red circle shows supercooled state, which phase transforms abruptly from a) 313 K to b) 312 K. The blue ellipse shows supercooled rectangular elements phase transforming from g) 303 K to h) 302 K.

cesses could be explained by the random distribution of nucleation centers resulting in different nucleation center amount per single disc. The number of nucleation centers in the discs which exhibit continuous phase transition should be higher than the number of nucleation centers in the disc which changes abruptly. A sufficient amount of the nucleation centers prevents supercooling and provides the continuous phase transition. The amounts of nucleation centers could affect the minimal supercooling temperature after which the FM-AF transition occurs. If the lateral dimension of a structure is reduced, the probability to have sufficient amount of nucleation centers is lowered and according to this idea, the smaller structures should show more pronounced supercooling than the larger ones.

This hypothesis was proven by the MFM measurement of an array consisting of 500 nm discs with the same FeRh thickness as the array from the previous measurement. This measurement was done for the cooling part of the hysteresis in the temperature range of 363–288 K by Dr. Jiří Liška. Part of the measurement is depicted in temperature range 363–305 K in Figure 4.5a-i. Only few discs – 3 out of 100, change continuously, one of them is marked by a green square in this figure. Other discs exhibit abrupt phase transition or they do not phase transform in this temperature range at all. A special

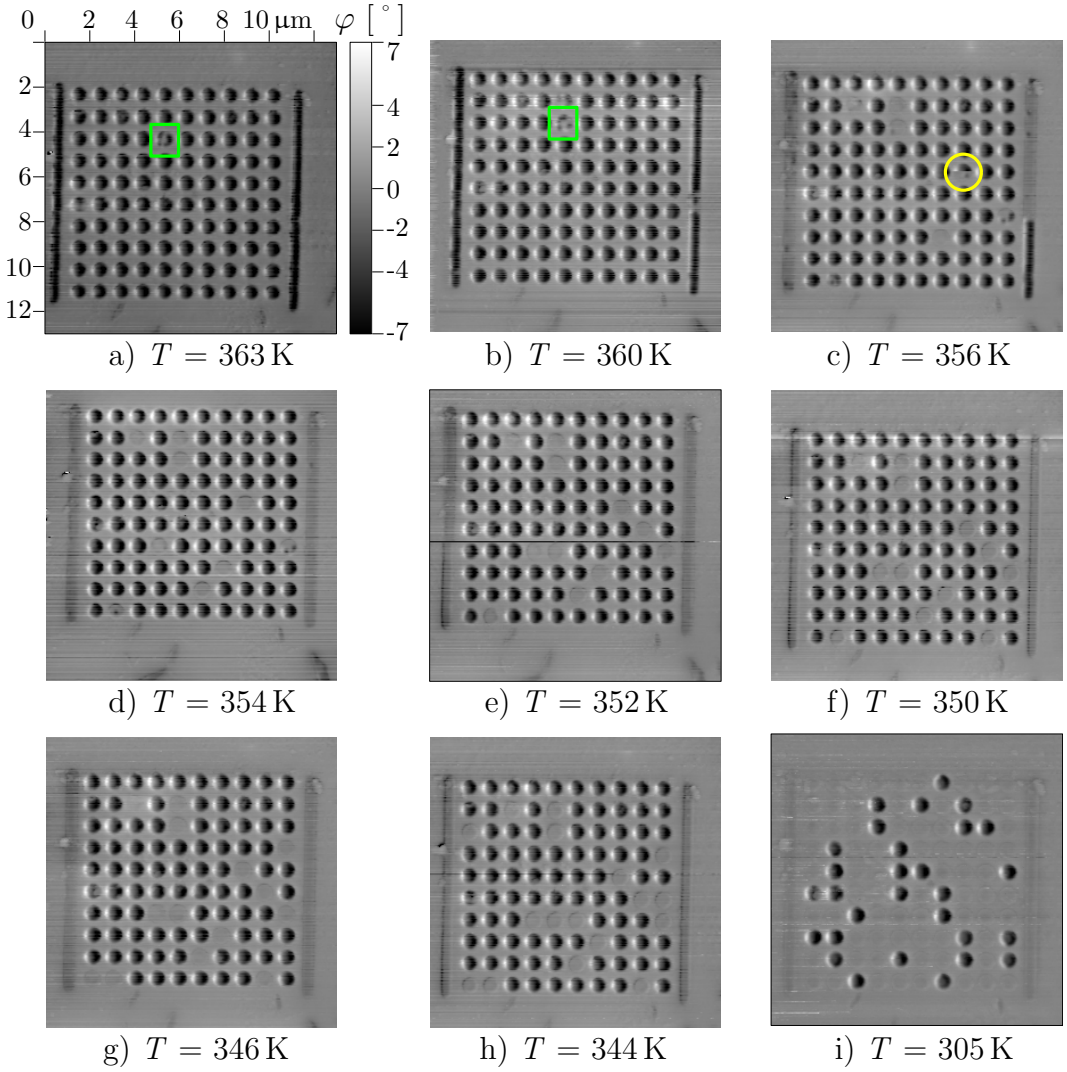

Figure 4.5: MFM measurement of the sample A26b with a 5 × 5 array of 500 nm discs. In the images a)–h), the FM-AF phase transition during cooling in the temperature range of 363–305 K is shown. The color phase was united for all of the images and is shown in a). The green square indicates the continuous phase transform during the cooling from a) 363 K to b) 360 K. The yellow circle shows the abrupt phase transition of the supercooled disc exactly during the scanning of the corresponding line. The measurement was performed by Dr. Jiří Liška.

event occurred in a disc marked by the yellow circle. The disc phase transformed exactly during the scanning of the corresponding line. This suggests that the phase transition in a sufficiently small structure could be stochastic with the mean time of nucleation events on the order of seconds and minutes, depending on the closeness of the actual temperature to the transition temperature. This supports the idea to capture the dynamics of the phase

transition by a resistance measurement, which has much higher sampling frequency than the MFM measurement.

The statistics of stochastic nucleation of the phase transition of 500 nm discs was obtained and evaluated by Dr.Jiří Liška. The idea was to analyze averaged MFM magnetic

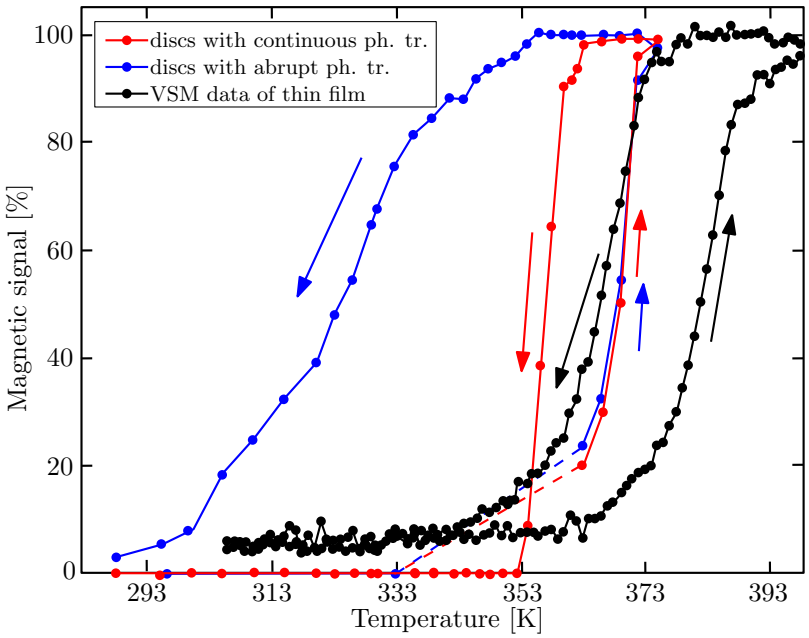

Figure 4.6: Comparison of averaged magnetic MFM signal of 500 nm discs and normalized VSM signal of original film. The red curve indicates the averaged magnetic signal of all the discs with the continuous phase transition. The blue curve marks the averaged signal of all the discs exhibiting average phase transition. The black curve corresponds to the normalized VSM signal of original film. Analysis made by Dr. Jiří Luška.

signal of all the discs which phase transform continuously and the signal of all the discs which phase transform abruptly. The results are shown in graph in Figure 4.6. The black curve corresponds to the normalized VSM measurement of the original film. The red curve shows similar width of the temperature hysteresis as in the normalized VSM measurement. The phase transition is shifted to the lower temperatures due to the lateral confinement, more discussed in the following sections. The heating curves are the same for both disc groups, while the cooling part of the discs which transform abruptly is significantly broadened due to the discs which do not transform and stay in the supercooled FM state. This may explain peculiar behavior of ultrathin FeRh films reported in [51], where the broadening effect of the temperature hysteresis upon cooling occurred. The reported ultrathin film was not homogeneous and the presence of nanoislands would cause a similar supercooling effect that we observe for disc arrays.

4.2.2. Transport measurements of stochastic nucleation

The transport measurements of stochastic nucleation were accompanied by many technical difficulties with the samples and the instrumentation. We experienced burning of the prepared 200 nm and 500 nm wide wires by a spark of the static discharge during the wire-bonding or during the manipulations with the sample, even with special precautions

taken. The damaged wires were attempted to be repaired by a combination of FIB milling and FIBID/FEBID technique, with no success.

However, before the terminal damage of the 500 nm wire, several measurement of stochastic nucleation were successful. The resistance measurement during the cooling with 0.2 K temperature step is shown in Figure 4.7a with several visible abrupt temperature steps. The biggest abrupt step with a magnitude $\approx 50\,\Omega$ occurred at the temperature of

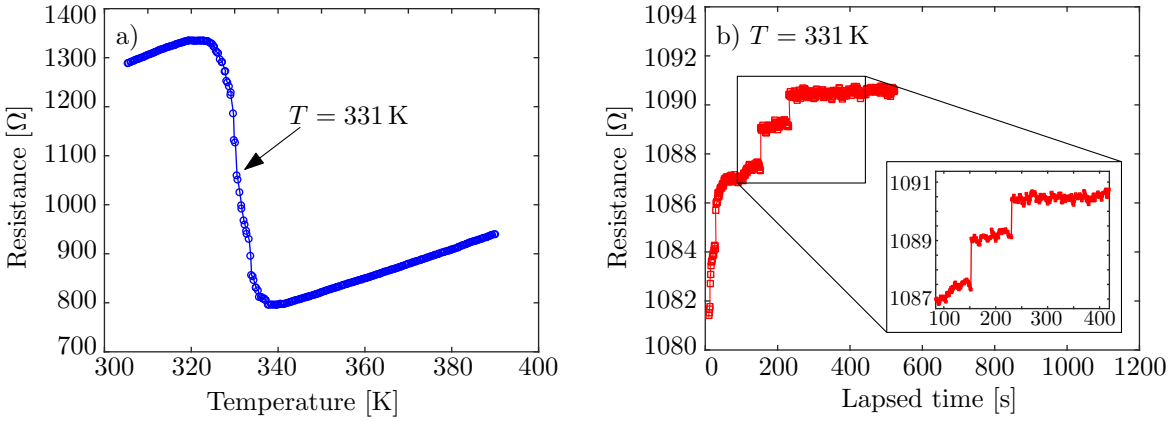

Figure 4.7: Transport measurement of the stochastic nucleation. a) Resistance during the cooling from 390 K. b) Time measurement of the resistance at $T = 331$ K. The detail shows the phase transitions of supercooled FM state to the AF state accompanied by the increase of resistance.

330 K. The experiment was set to detect this step, and the procedures ran as described in the subsection 3.4.1. The sample was heated to 390 K to the fully FM state. Then the sample was cooled to the vicinity of the step transition at 331 K. The resulting resistance vs time measurement is depicted in Figure 4.7b. The beginning of the graph shows continuous growth of resistance, as the sample was heated slower than the temperature sensor. The temperature was stable after ≈ 70 s. Afterwards two abrupt phase transitions occurred with the resistance of $\approx 1{-}2\,\Omega$. The awaited $\approx 50\,\Omega$ step did not occur during the measured time range of 500 s. After this measurement, the resistance measurement started to be unstable. The instability was probably introduced by an inappropriate thermal contact between the sample and the temperature stage provided by a copper double-sided tape. After the tape replacement and further wire-bonding, the 500 nm wide wire could not be measured due to the problems with static discharges.

We observed that the phase transition dynamics occurs on the order of minutes, depending on how close the actual temperature is to the critical one. Proper sample, safer handling and more statistics could bring the information about the mean nucleation time with subsequent determination of the energy barrier between the AF and FM state in supercooled FeRh wires.

4.3. Correlation length of phase domains

The correlation length of phase domains in thin films and in patterned structures was estimated by a combination of MFM imaging and postprocessing of measured data by HHCF analysis. The results are discussed in the following sections.

4.3.1. Thin films

Investigation of film thickness influence on the phase transition properties and the phase domain sizes was done by measuring two different FeRh film with thicknesses 200 nm and 36 nm. *MFM lift height* parameter was set to 80 nm and the 11 μm scan size was chosen on a $(256 \times 256)\,\mathrm{px}^2$ scanning window.

Measurement of a 200-nm film on the sample P17b was processed by a Python3 script, which allows to manually choose a non-magnetic area to calculate the non-magnetic median which should be a common value for the entire set of measurements. This non-magnetic area corresponds to the area of the central defect. After adjustment of the measurements to one non-magnetic value, a unified phase scale was set. The phase transitions from AF to FM and from FM to AF were measured in the temperature range of 333–378K, with 41 temperature steps. In Figure 4.8, a part of the cooling and a part of the heating measurement cycle is shown. Figures 4.8a-f show the phase transition during cooling from 371 K to 359 K. The phase transition from FM to AF extends from the nucleation center location – the defect depicted in the middle of the images. During further cooling, new AF domains nucleated and all AF domains grew. On the other hand, Figures 4.8g-n depict the AF-FM phase transition during heating from 363 K to 375 K. Massive nucleation of new domains occurred upon heating from 363 K to 364 K. The following heating was accompanied by further nucleation of FM domains and by their growth in the direction towards the defect in the middle. Both phase transitions have in common that nucleation proceeds in a specific direction given by the sample's diagonals. This anisotropy is induced by the crystalline orientation of the FeRh lattice on MgO(001) substrate, which is rotated by 45°. In films with larger thicknesses, the anisotropy starts to play a role in the nucleation and the growth direction.

The measurement of phase transition in a 36-nm-thick film on the sample A21 was processed differently. The same procedure as in the case of P17b could not be used, since the non-magnetic area of the defect was much smaller than in the case of P17b. Hence, the whole set was processed by the Gwyddion software in only one step – by selection of the minimum and the maximum value for the color scale in each image. A21 was measured for the heating part of the hysteresis loop in the temperature range from 353 K to 367 K including the whole process of the FM-AF phase transition. The cooling part was measured only in the interval of 363–355 K due to the tip damage. The total number of temperature steps in the cooling measurement was 9 and during the heating it was 11. Figures 4.9a-c) depict part of the cooling loop. The process of the FM-AF phase transition in 36 nm thin film is similar to the process in the one occuring in thicker sample. The growing starts from the defects and from much higher number of nucleation centers than in the case of 200 nm thick film. In Figures 4.9d-i, the part of the heating loop is shown in the temperature range of 358–363 K. The phase transition proceeds through the nucleation of domains much smaller than the domains in the 200 nm thick film. The FM domains nucleate in domain clusters.

HHCF analysis of thin films

The measured data were processed by methods described in the subsection 3.3.2. By fitting, two characteristic values of each measurement at specific temperature were obtained – the correlation length ξ characterizing the average domain size and the magnetic roughness σ, which gives the information about the contrast. The non-magnetic defect in the middle played a role in the HHCF analysis of P17b results, hence the square area

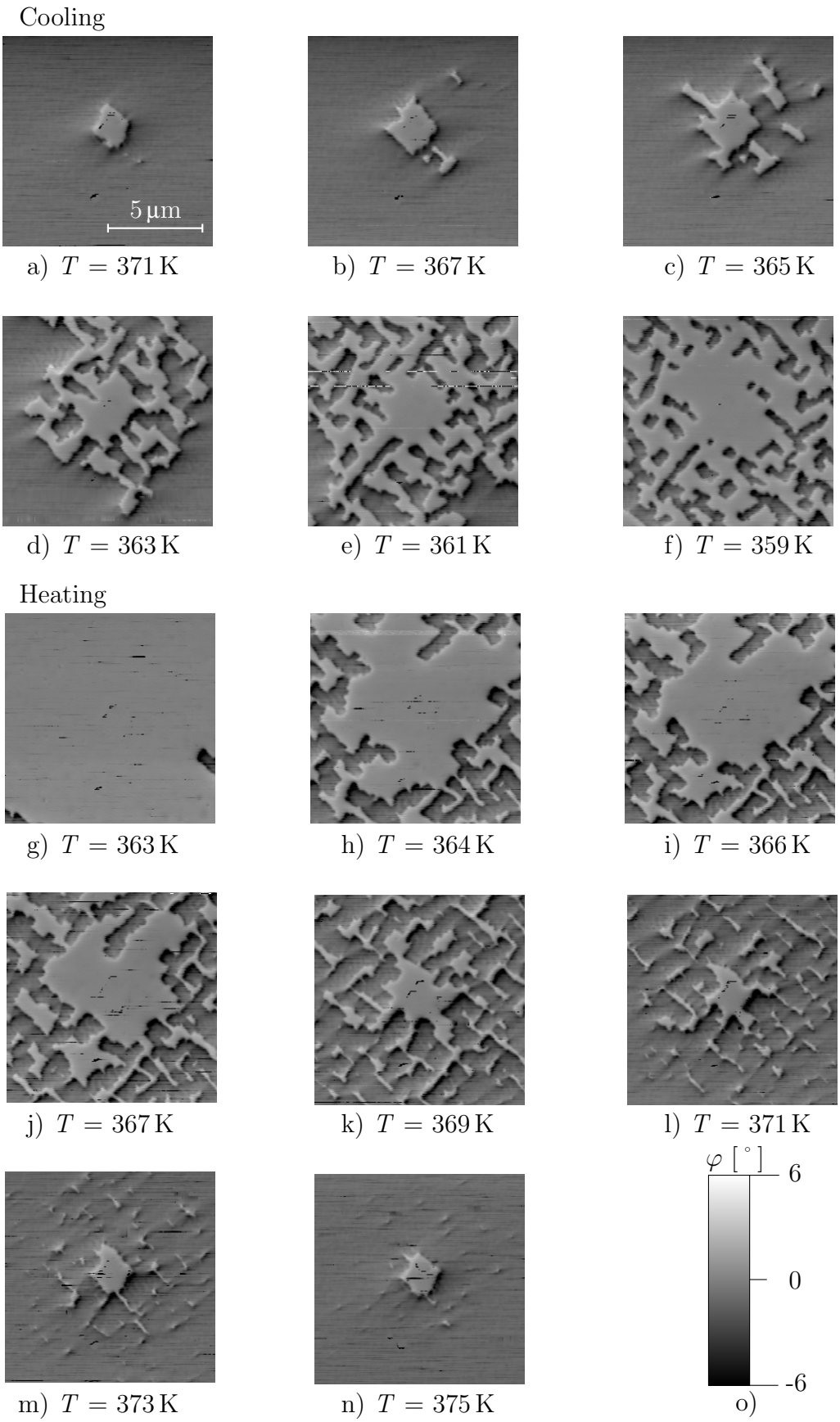

Figure 4.8: MFM measurement of the phase transition in 200 nm film on the sample P17b. a-f) Phase transition during cooling from 371 K to 359 K. g-n) Phase transition during heating from 363 K to 375 K. o) Unified colour scale same for all of the images.

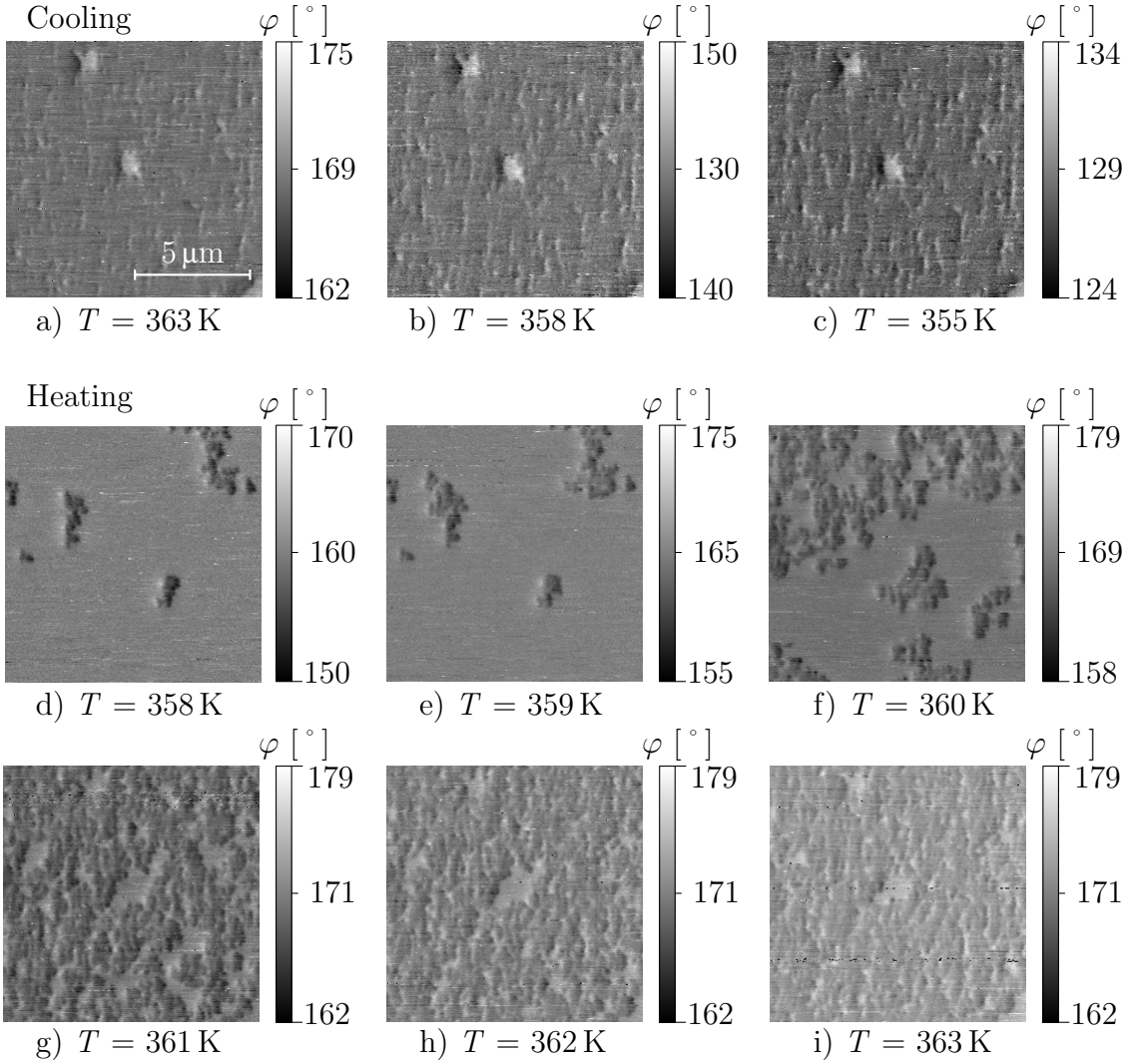

Figure 4.9: MFM measurement of the phase transition in 36 nm thick film on sample A21. a-c) Cooling from 363 K to 355 K. d-i) Heating from 358 K to 363 K.

with the size of 4 µm without defect was chosen for the next processing and fitting, as marked in Figure 4.8g. In the sample A21 the size of defect was negligible, hence the whole area was taken into account. The correlation length and the magnetic roughness are plotted as functions of temperature in Figure 4.10 for the two sets of the thin films measurements, together with their VSM characterization. To compare the temperature dependence of the HHCF parameters with the VSM measurement, the HHCF parametres were shifted by the 8 K/T due to the presence of the out-of-plane magnetic field in MFM measurements.

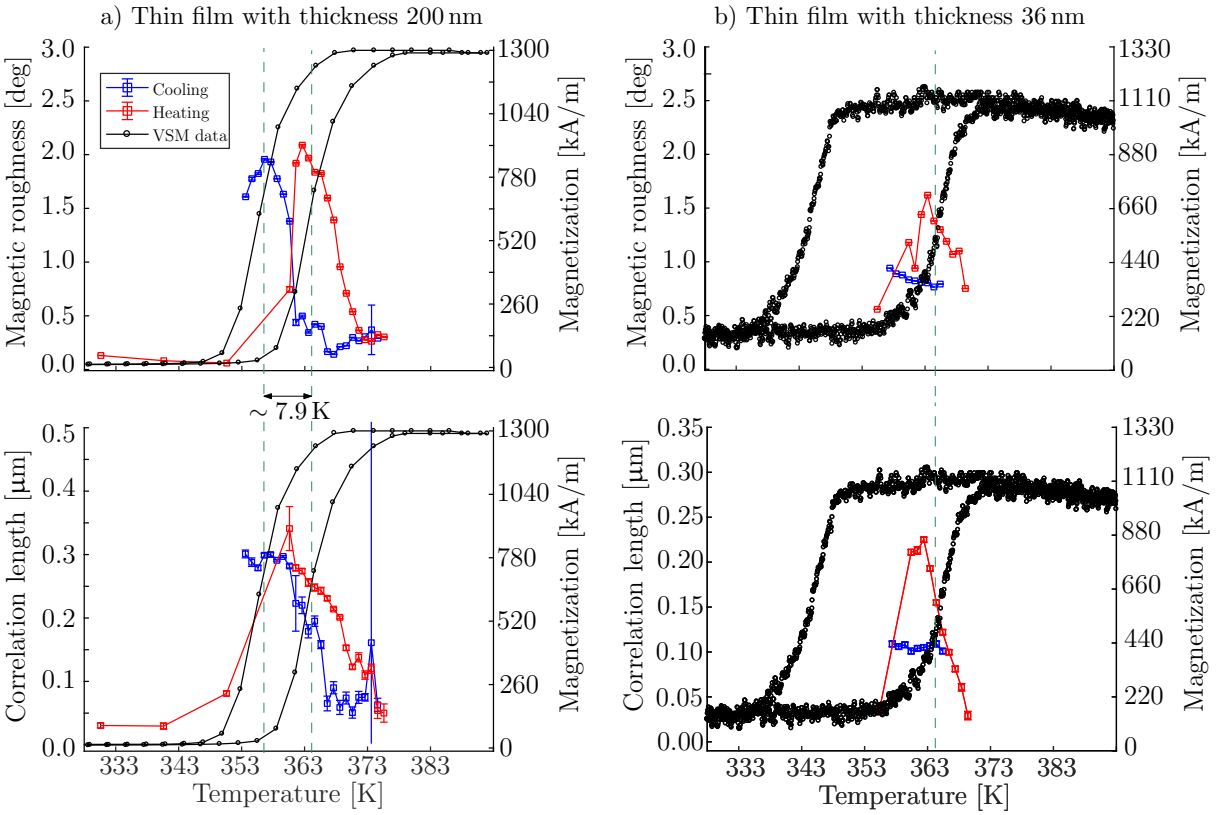

Figure 4.10: HHCF analysis of the thin films measurement, including temperature dependence of the magnetic roughness and the correlation length. a) 200 nm thick film on the sample P17b. b) 36 nm thick fim on the sample A21, the cooling part is incomplete due to the tip damage. The green dashed lines indicates the magnetic roughness maxima.

Figure 4.10a shows the HHCF analysis of the 200-nm film temperature measurement. Firstly, the temperature dependence of the magnetic roughness will be discussed. Deeply in the AF state, no magnetic signal is detected, hence the roughness is close to the noise level < 0.2deg. As the FM domains nucleate, the magnetic roughness grows to its maximum at maximal phase separation. After surpassing of this maximum, the measured area starts to fill with magnetic domains and the magnetic roughness decreases. When the area is fully FM, the magnetic roughness is again close to the noise level. Similarly, the correlation length grows with nucleation of new domains towards the maximal phase separation and as FM domains fill the area completely, the correlation length decreases. The same situation occured for a 36-nm film shown in Figure 4.10b.

The correlation length for maximal phase separation during the cooling is (299 ± 3) nm and during the heating (248 ± 6) nm for a film with 200-nm thickness. The average size of domains at maximal phase separation during the FM-AF transition is bigger than during

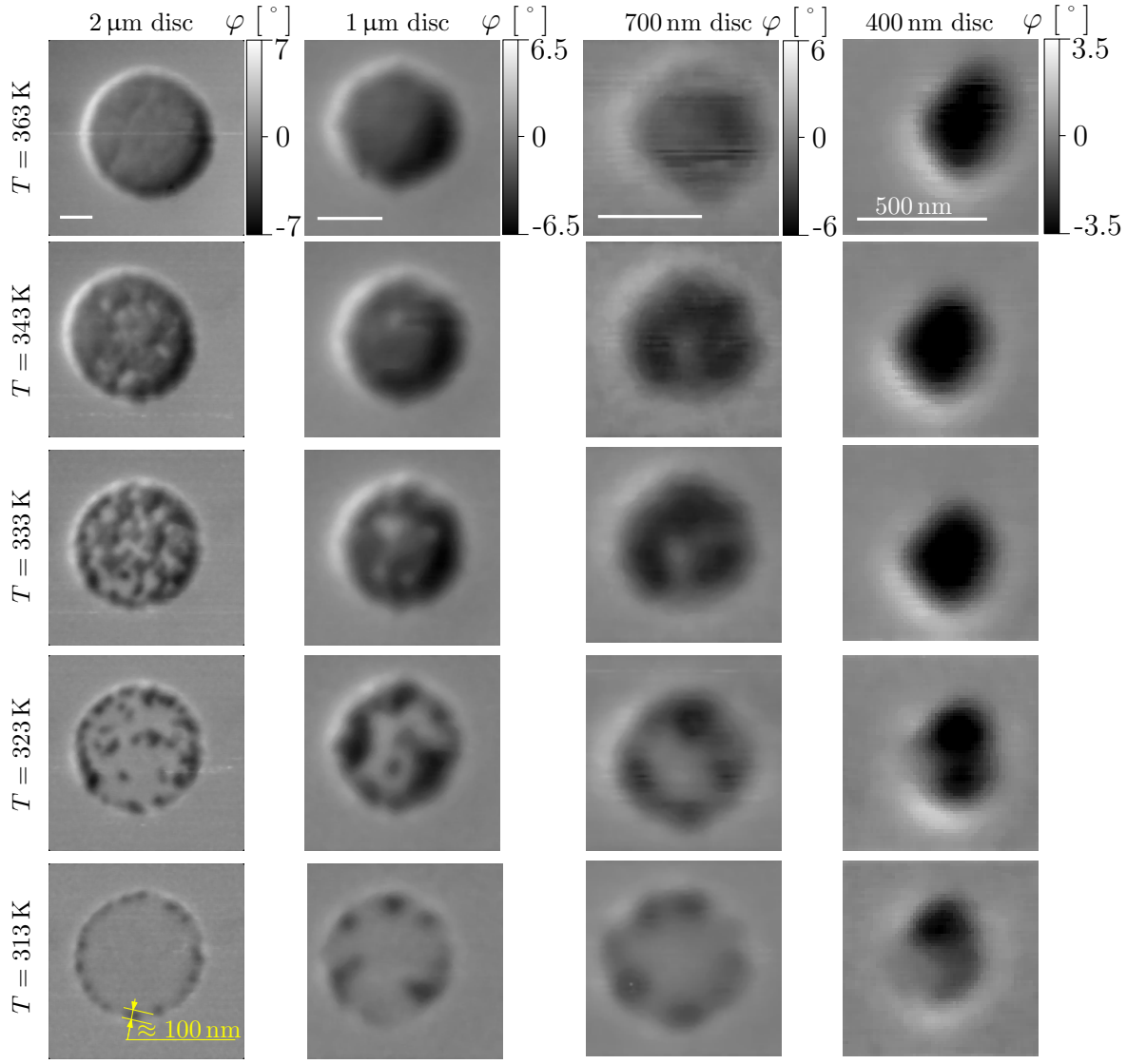

Figure 4.11: MFM measurements comparison for discs with sizes of 2 µm, 1 µm, 700 nm and 400 nm during cooling from 363 K to 313 K. White lateral scale bar corresponds to 500 nm in all images.

the AF-FM phase transition, referring to the theory that FM domains are stabilizing each other. For the thinner film of 36 nm the correlation length for maximal phase separation during heating was lower (155 ± 3) nm. This is consistent with MFM observation that domains in the thinner film were smaller. The FM domains in the thicker film are larger because the homogeneity of the thicker film is higher. The influence of the defects and the dislocations driving the size of the domains is lower in case of the thicker film.

4.3.2. Patterns

The influence of the lateral confinement on the phase transition and the size of the domains was investigated by measuring patterned discs with sizes 2 µm, 1 µm, 700 nm and 400 nm on the sample X79b and by a HHCF analysis of measured data.

The measurements were done using the *MFM lift height* 100 nm above the sample's topography using a 256 px scan size corresponding to 3 µm. This results in ≈ 11.7 nm real pixel size. The 2 µm disc was measured in a square scanning window, while all

other discs were measured in a rectangular scanning windows with aspect ratios 2, 3 and 4, respectively. The phase transition was captured in the temperature range 288–363 K for both – the heating cycle and the cooling cycle. Measurements were processed by the method discussed above in the subsection 3.3.1. Figure 4.11 shows comparison of MFM measurements of all discs during cooling from 363 K to 313 K. The FM-AF phase transition during cooling proceeds from the center to the edges of the discs with an exception for a 400 nm discs, which at 363 K only consists from one single phase state and during the cooling decays to the two FM domains state and further cooling leads to a fully transformed to AF state.

It is apparent from the images, that the lateral confinement of the structure – the reduction of its size – shifts the transition temperature to the lower values. The same applies to the heating cycle where the phase transition starts from the ferromagnetic edges with width of $\approx$ 100 nm which provide nucleation centers for further FM domain growth. During further heating, the phase transition proceeds towards the middle of the disc. FM edges occurred due to the strain relaxation on the structure edges. The strain relaxation effect could be related to the action of substrate compressing or expanding the FeRh lattice in a thin film, which vanishes at the structure boundaries.

HHCF analysis of patterns

The HHCF analysis of individual 2 μm, 1 μm, 700 nm and 400 nm disc was done in a square region with a size of 256, 128, 80, 64 px, respectively, which closes the entire structure in the region of interest. The construction of HHCF and its fitting was done similarly as in the case of thin layers resulting in the temperature dependence of the correlation length ξ and magnetic roughness σ. The difference occurs in their interpretation. In the case of thin films, as the temperature increases, the magnetic roughness grows from the noise level to its maximum at the temperature of maximal phase separation and then decreases to the noise level, as the area fills with FM domains. In the case of structures, a wider

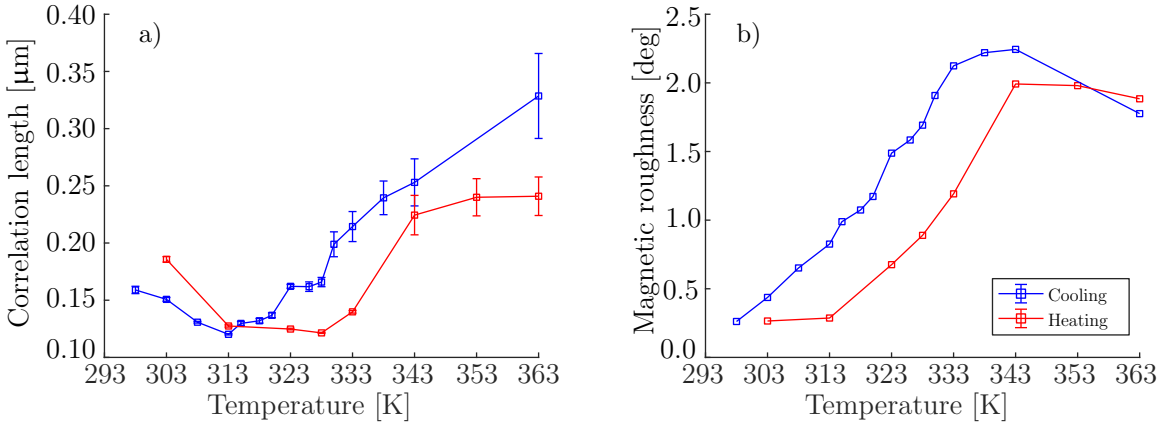

Figure 4.12: Temperature dependence of HHCF parametres during cooling and heating of the disc with a diameter of 700 nm. a) Correlation length ξ b) Magnetic roughness σ.

hysteresis is expected. The magnetic roughness grows with the FM domains nucleation but its maximum will not be at the maximal phase separation temperature, but will raise to the temperature when the disc is fully transformed to the FM state, where the disc looks as one homogeneous FM domain in the non-magnetic background. After further temperature increasing, the magnetic roughness remains constant. This is illustrated in

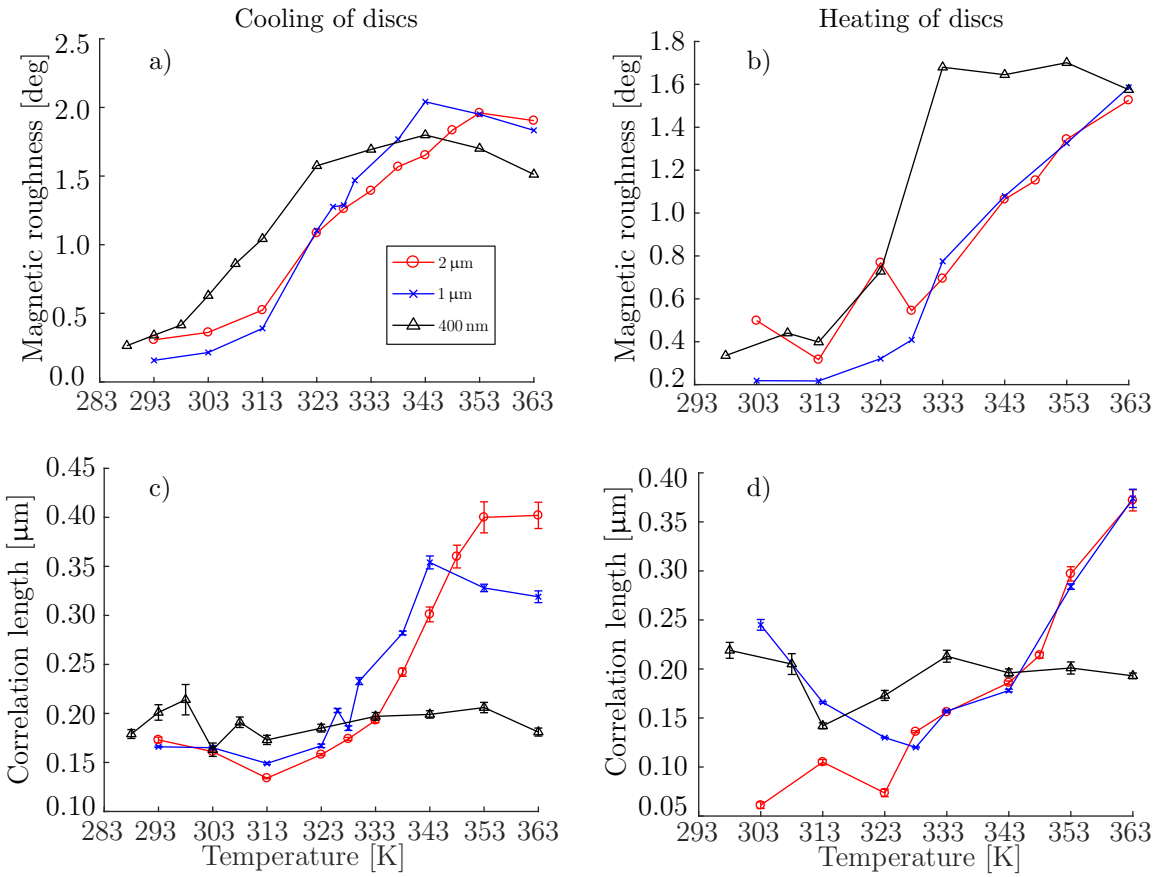

Figure 4.13: Temperature dependence of HHCF parameters for discs with diameters of 2 µm, 1 µm and 400 nm. a) Magnetic roughness during cooling. b) Magnetic roughness during heating. c) Correlation length during cooling. d) Correlation length during heating.

Figure 4.12b for the cooling and the heating part of the phase transition in 700-nm disc. The correlation length is shown in Figure 4.12a and for the fully FM phase it is influenced by a factor related to the finite size of the discs. The temperature dependence of the correlation length indicates that the domain structure changes continuously, showing a minimum at the maximal phase separation, where the average size of the phase domains can be determined. In the fully AF state, the correlation length increases again, but this increase corresponds to small variations of the signal unrelated to the large magnetic roughness in case of the phase domain separation (see vanishing magnetic roughness for lowest temperatures in Figure 4.12b).

The temperature dependency of the correlation length and the magnetic roughness for all of the other measured discs with diameters 2 µm, 1 µm and 400 n are depicted in Figure 4.13. The temperature dependence of the magnetic roughness (depicted in Figures 4.13a,b) quantitatively prove that the transition temperatures shift to the lower temperatures for smaller structures. The magnetic roughness saturates during the heating only for the 400 nm discs. This corresponds to the fact that only the disc with a 400-nm diameter fully phase transformed to the FM state during the heating in measured temperature range. On the other hand, the disc with the diameter of 400 nm did not fully transform to the AF state during the cooling, while the 2 µm and the 1 µm disc did. This suggests that the full hysteresis loop was not measured within the experimental temperature range. Figures 4.13c-d depict the temperature dependency of the correlation length during the

cooling and the heating, respectively. The correlation lengths are influenced by the finite size of the disc, as it is apparent in Figure 4.13c, where the correlation length is at 363 K is maximal and proportional to the disc diameter. At the maximal phase separation it is possible to compare the correlation lengths of phase domains for different structure sizes. We observe a trend of increasing correlation length of phase domains with decreasing the structure size, however to improve the interpretation, more temperature steps and larger statistics are needed.

Conclusion

The main objective of this work was investigation of the spatial confinement effects on the phase transition and the sizes of the phase domains in FeRh structures. Firstly, we studied the supercooling effect in patterned arrays of FeRh discs with diameters of 700 nm and 500 nm. The arrays were imaged by MFM during the phase transition and several different scenarios were identified. The measurement of 700-nm-wide discs showed that the discs underwent the phase transition continuously, abruptly or the phase transition did not happen at all. The abrupt phase transition is connected to the supercooling phenomenon and depends on the number of nucleation sites in the structure, whether the disc changes through the continuous phase transition by breaking into a multidomain structure or transforming abruptly from the supercooled state. This findings were reinforced by the MFM measurement of 500-nm discs at varying temperature. This measurement demonstrated that the discs with a smaller diameter are much more sensitive to the supercooling phenomenon. The phase transition from the metastable supercooled state occurred in order of minutes. The statistics of the average MFM signal of all the discs transforming abruptly shows the broadening of the hysteresis loop due to the supercooled discs in the FM state.

Further experiments focused on the effect of FeRh film thickness on the phase transition and the phase domain sizes. The phase transition was observed by MFM imaging and several qualitative results were discussed. The AF-FM phase transition nucleates and grows towards defects, while the FM-AF phase transition starts and spreads away from defects. The domain nucleation and growth direction is strongly influenced by the crystalline anisotropy which was introduced by the FeRh lattice rotation at the MgO(001) substrate. The quantitative results were obtained using HHCF analysis and the resulting correlation lengths at maximal phase separation for a 200-nm-thick film are (299 ± 3) nm during cooling and (248 ± 6) nm during heating. This confirms the hypothesis that the FM state features longer-distance correlations compared to the AF state during the phase transition. The correlation length for the 36-nm-thick film was found to be (155 ± 3) nm, which is consistent with the qualitative observation that the domains in thicker sample are larger. This is caused by the higher homogeneity of the thicker film.

The last set of experiments dealt with the effects of lateral confinement on the phase transition and the hase domain sizes. The AF-FM phase transition proceeded from the disc edges to the center, while the FM-AF phase transition proceeds from the middle to the edges. The FM edges occurred due to the strain relaxation at the structure boundary. The strain relaxation effect could be related to the action of substrate compressing or expanding the FeRh lattice in a thin film, which vanishes at the structure boundaries. The strain relaxation shifts the temperature of the whole transition and is consistent with the fact that the phase transition temperature decreases as the diameter of the structure decreases. The HHCF analysis showed a trend of increasing correlation length of phase

domains with decreasing the structure size, however to improve the interpretation, more temperature steps and larger statistics are needed.

The MFM measurement could be improved by using tips with higher resolution or by enlarging the scan size, for the price that the single measurement will take more time. Future experiments will also focus on the transport measurement of stochastic nucleation on wire which exhibits single-step phase transition. The larger statistics could tell more about the system dynamics.

References

1. Fallot, M. & Hocart, R. Sur lapparition du ferromagnétisme par elevation de temperature dans des alliages de fer et de rhodium. *Revue Scientifique* **77,** 498–499 (1939).
2. Geschneidner, K. & Pecharsky, V. Thirty years of near room temperature magnetic cooling: Where we are today and future prospects. *International Journal of Refrigeration* **31,** 945–961 (2008).
3. Thiele, J. *et al.* Magnetic and structural properties of FePt-FeRh exchange spring films for thermally assisted magnetic recording media. *IEEE Transactions on Magnetics* **40,** 2537–2542 (2004).
4. Kryder, M. H. *et al.* Heat Assisted Magnetic Recording. *Proceedings of the IEEE* **96,** 1810–1835 (2008).
5. Uhlíř, V., Arregi, J. A. & Fullerton, E. E. Colossal magnetic phase transition asymmetry in mesoscale FeRh stripes. *Nature Communications* **7,** 13113 (2016).
6. Jaskowiec, J. *Mikroskopie magnetických sil a transportní vlastnosti metamagnetických nanostruktur.* Bakalářská práce (Vysoké učení technické v Brně. Fakulta strojního inženýrství, Brno, 2017).
7. Schánilec, V. *Magnetická fázová přeměna v prostorově omezených strukturách.* Bakalářská práce (Vysoké učení technické v Brně. Fakulta strojního inženýrství, 2016).
8. Halliday, D., Resnick, R. & Walker, J. *Fyzika* 2nd ed. 1248 pp. ISBN: 9788021441231 (VUTIUM, Brno, 2013).
9. Coey, J. M. D. *Magnetism and Magnetic Materials* 614. ISBN: 9781139486927 (Cambridge University Press, Cambridge, 2010).
10. Blundell, S. *Magnetism in Condensed Matter* 256. ISBN: 9780198505914 (Oxford University Press, Oxford, 2001).
11. Guimaraes, A. P. *Principles of Nanomagnetism* 224. ISBN: 9783642261114 (Springer-Verlag Berlin Heidelberg, Berlin, 2009).
12. Stöhr, J. & Siegmann, H. C. *Magnetism: From fundamentals to nanoscale dynamics* 822. ISBN: 9783540302834 (Springer, Berlin, 2006).
13. Wojewoda, O. *Disperzní relace magnonických krystalů s netriviální prostorovou distribucí magnetické anizotropie.* Bakalářská práce (Vysoké učení technické v Brně, Fakulta strojního inženýrství, Brno, 2018).
14. Kittel, C. *Introduction to solid state physics* 8th ed., 688. ISBN: 9780471415268 (Wiley, Hoboken, NJ, 2005).

15. Fruchart, O. *Lecture notes on Nanomagnetism* `http://fruchart.eu/olivier/publications/index.html` (2019).

16. Jiles, D. *Introduction to Magnetism and Magnetic Materials* 3rd ed. ISBN: 9781482238877 (CRC Press, Taylor and Francis Group, Boca Raton, 2016).

17. Sethna, J. *Statistical Mechanics: Entropy, Order Parameters, and Complexity* 966 pp. ISBN: 9780198566762 (OUP Oxford, New York, 2006).

18. Papon, P. *et al. The physics of phase transitions* ISBN: 9783540333890 (Springer, New York, 2006).

19. EDWARDS, G. R., EVANS, L. F. & HAMANN, S. D. Nucleation of Ice by Mechanical Shock. *Nature* **223,** 390–391 (1969).

20. Lewis, L. H., Marrows, C. H. & Langridge, S. Coupled magnetic, structural, and electronic phase transitions in FeRh. *Journal of Physics D: Applied Physics* **49,** 323002 (2016).

21. Motyčková, L. *Epitaxial growth and characterization of metamagnetic nanoparticles for biomedical applications.* Bachelor thesis (Vysoké učení technické v Brně. Fakulta strojního inženýrství, Brno, 2018).

22. Fabiánová, K. *Magnetotransport properties of FeRh nanowires.* Diploma thesis (Vysoké učení technické v Brně. Fakulta strojního inženýrství, Brno, 2018).

23. Swartzendruber, L. J. The Fe-Rh (Iron-Rhodium) system. *Bulletin of Alloy Phase Diagrams* **5,** 456–462 (1984).

24. Zakharov, A. I. *et al.* Magnetic and magnetoelastic properties of a metamagnetic iron-rhodium alloy. *Journal of Experimental and Theoretical Physics* **19,** 1348–1353 (1964).

25. Rosenberg, M. *et al.* A Mössbauer spectroscopy and magnetic study of FeRh. *Journal of Magnetism and Magnetic Materials* **177-181,** 135–136 (1998).

26. Shirane, G., Nathans, R. & Chen, C. W. Magnetic moments and unpaired spin densities in the Fe-Rh alloys. *Physical Review* **134,** A1547 (1964).

27. Maat, S., Thiele, J. & Fullerton, E. E. Temperature and field hysteresis of the antiferromagnetic-to-ferromagnetic phase transition in epitaxial FeRh films. *Physical Review B* **72,** 214432 (2005).

28. Kouvel, J. S. Unusual nature of the abrupt magnetic transition in FeRh and its pseudobinary variants. *Journal of Applied Physics* **37,** 1257–1258 (1966).

29. Moruzzi, V. L. & Marcus, P. M. Antiferromagnetic-ferromagnetic transition in FeRh. *Physical Review B* **46,** 2864–2873 (1992).

30. Wayne, R. C. Pressure Dependence of the Magnetic Transitions in Fe-Rh Alloys. *Physical Review* **170,** 523–527 (1967).

31. Manekar, M., Mukherjee, C. & Roy, S. B. Imaging of time evolution of the first-order magneto-structural transition in Fe-Rh alloy using magnetic force microscopy. *A Letters Journal Exploring The Frontiers of Physics* **80,** 17004 (2007).

32. Shao, J. *et al.* Emerging single-phase state in small manganite nanodisks. *Proceedings of the National Academy of Sciences* **133,** 9228–9231 (2016).

33. Arregi, J. A. *et al.* Magnetization reversal and confinement effects across the metamagnetic phase transition in mesoscale FeRh structures. *Journal of Physics D: Applied Physics* **51,** 105001 (2018).

34. Temple, R. C. *et al.* Antiferromagnetic-ferromagnetic phase domain development in nanopatterned FeRh islands. *Phys. Rev. Materials* **2,** 104406 (10 2018).

35. Keavney, D. J. *et al.* Phase Coexistence and Kinetic Arrest in the Magnetostructural Transition of the Ordered Alloy FeRh. *Scientific Reports* **8,** 1778 (1 2018).

36. Hajducek, J. *Nukleace magnetické fázové přeměny v nanostrukturách řízená substrátem.* Bakalářská práce (Vysoké učení technické v Brně. Fakulta strojního inženýrství, Brno, 2019).

37. Hubert, A., Schäfer, R. & Rudolf Schafer, A. *Magnetic Domains: The Analysis of Magnetic Microstructures* ISBN: 9783540641087 (Springer, 1998).

38. Hopster, H. & Oepen, H. *Magnetic Microscopy of Nanostructures* ISBN: 9783540266419 (2006).

39. Abelmann, L. *et al.* Comparing the resolution of magnetic force microscopes using the CAMST reference samples. *Journal of Magnetism and Magnetic Materials* **190,** 135–147 (1998).

40. Nečas, D. *et al.* Determination of tip transfer function for quantitative MFM using frequency domain filtering and least squares method. *Scientific Reports* **9,** 3880 (2019).

41. Staňo, M. *Characterization of magnetic nanostructures by magnetic force microscopy.* Master's thesis (Brno University of Technology. Faculty of Mechanical Engineering, Brno, 2014).

42. Turčan, I. *Mikroskopie magnetických sil v proměnném magnetickém poli.* Bakalářská práce (Vysoké učení technické v Brně. Fakulta strojního inženýrství, Brno, 2015).

43. Kaemmar, S. B. *Introduction to Bruker's ScanAsyst and PeakForce Tapping AFM Technology* Rev. A0. Bruker (2011), 12.

44. Dumas, P. *et al.* Quantitative Microroughness Analysis down to the Nanometer Scale. *Europhysics Letters (EPL)* **22,** 717–722 (June 1993).

45. Nečas, D. & Klapetek, P. One-dimensional autocorrelation and power spectrum density functions of irregular regions. *Ultramicroscopy* **124,** 13–19 (2013).

46. Gredig, T., Silverstein, E. A. & Byrne, M. P. Height-Height Correlation Function to Determine Grain Size in Iron Phthalocyanine Thin Films. *Journal of Physics: Conference Series* **417,** 012069 (Mar. 2013).

47. Nečas, D. & Klapetek, P. Gwyddion: an open-source software for SPM data analysis. *Central European Journal of Physics* **10,** 181–188 (1 2012).

48. Dunn Patrick F nd Davis, M. P. *Measurement and Data Analysis for Engineering and Science* 576 pp. ISBN: 9781138050860 (CRC Press, Boca Raton, 2017).

49. Uhlíř, V. *et al.* Current-induced domain wall motion and magnetization dynamics in CoFeB/Cu/Co nanostripes. *Journal of Physics: Condensed Matter* **24,** 024213 (2011).

50. Bertotti, G. *Hysteresis in Magnetism* 558 pp. ISBN: 9780080534374 (Academic Press, New York, 1998).

51. Han, G. C. *et al.* Magnetic stability of ultrathin FeRh films. *Journal of Applied Physics* **113,** 17C107 (2013).

52. Gholaminejad, A. A Study of Water Supercooling. *Journal of Electronics Cooling and Thermal Control* **3,** 1–6 (2013).

List of abbreviations

AC	Alternate Current
ACF	Autocorrelation function
AF	Antiferromagnetic, Antiferromagnetic phase/domain
AF-FM	Phase transition from AF to FM
AFM	Atomic Force Microscopy
DAQ	Data Acquisition (DAQ card)
DC	Direct Current
EBL	Electron Beam Lithography
FEBID	Focused Electron Beam Induced Deposition
FeRh	Iron-Rhodium
FIB	Focused Ion Beam
FIBID	Focused Ion Beam Induced Deposition
FM	Ferromagnetic, Ferromagnetic phase/domain
FM-AF	Phase transition from FM to AF
HAMR	Heat Assisted Magnetic Recording
HHCF	Height-Height Correlation Function
LPCMO	$La_{0.325}Pr_{0.3}Ca_{0.375}MnO_3$
MESP	Magnetic tips used in this work
MFM	Magnetic Force Microscopy
MOKE	Magneto-optical Kerr Effect
PF	PeakForce
PID	Propotional, Integrational, Differential regulation
PVD	Physical Vapour Deposition

SPM	Scanning Probe Microscopy
TTF	Tip Transfer Function
VSM	Vibrating Sample Magnetometry
XMCD	X-ray Magnetic Circular Dichroism
XRR	X-ray Reflection

List of attachments

MATLAB Scripts

- `hhcfcalculation.m` – This script was used for the HHCF information calculation. The 2D HHCF was calculated using two *for* cycles. The 1D HHCF information was calculated by sorting the matrix elements to the vectors, described in the subsection 3.3.2. The user interface allows to manually select data for processing. The output 2D HHCF is saved to the grayscale png image and 1D HHCF to the txt file.
- `reducer.m` – This simple script was used to select first several hundreds of data to speed up fitting. The script offers user interface to select data for processing and the reduced results are saved to the txt file.
- `cropper.m` – This simple script was used to select the same square area from the whole set of measurements. The script offers user interface to select data for processing and the output is saved to the grayscale png image.

Python3 Scripts

- `fitter.py` – This script was used to fit the HHCF data created by the script `hhcfcalculation.m`. The user interface allows to manually select data to fit and it provides the manual selection of interval to fit. The output is png graphs with fitted function and the txt file containing fitted parameters.
- `median_scaling.py` – This script was used to adjust all measurements to the median of calculated from manually selected square area. The user interface allows to manually select data for processing. The input data are in the gwy file and the output are the png files.